Bayesian Retrieval of Complete Posterior PDFs of Oceanic Rain Rate From Microwave Observations

J. Christine Chiu[a] and Grant W. Petty[b]

[a]Joint Center for Earth Systems Technology

University of Maryland Baltimore County, Baltimore, Maryland

[b]Department of Atmospheric and Oceanic Sciences

University of Wisconsin, Madison, Wisconsin

Submitted May 2005; revised December 2005

Corresponding author address: J. Christine Chiu, NASA/GSFC, Code 613.2, Greenbelt, MD 20771, cchiu@climate.gsfc.nasa.gov, Tel. 301-614-6816, FAX 301-614-6307

Abstract

This paper presents a new Bayesian algorithm for retrieving surface rain rate from Tropical Rainfall Measurements Mission (TRMM) Microwave Imager (TMI) over the ocean, along with validations against estimates from the TRMM Precipitation Radar (PR). The Bayesian approach offers a rigorous basis for optimally combining multichannel observations with prior knowledge. While other rain rate algorithms have been published that are based at least partly on Bayesian reasoning, this is believed to be the first self-contained algorithm that fully exploits Bayes' Theorem to yield not just a single rain rate, but rather a continuous posterior probability distribution of rain rate.

To advance our understanding of theoretical benefits of the Bayesian approach, we have conducted sensitivity analyses based on two synthetic datasets for which the "true" conditional and prior distribution are known. Results demonstrate that even when the prior and conditional likelihoods are specified perfectly, biased retrievals may occur at high rain rates. This bias is not the result of a defect of the Bayesian formalism but rather represents the expected outcome when the physical constraint imposed by the radiometric observations is weak, due to saturation effects. It is also suggested that the choice of the estimators and the prior information are both crucial to the retrieval. In addition, the performance of our Bayesian algorithm is found to be comparable to that of other benchmark algorithms in real-world applications, while having the additional advantage of providing a complete continuous posterior probability distribution of surface rain rate.

1. Introduction

Satellite passive microwave observations are now widely used to estimate global surface rainfall (Adler et al. 2001). Inference of surface rainfall R from microwave brightness temperatures T_B would be less troublesome if the relationship between these two variables were unique and reasonably linear. Unfortunately, not only is the relationship nonmonotonic owing to the competing effects of scattering and emission (Petty 1994a), but a variety of microphysical and environmental factors introduces significant variability into the relationship. This ambiguity is compounded by spatial variability in the rain intensity when the strongly nonlinear function of local rain rate is averaged over a finite instrument field-of-view (FOV) of order 10 km or larger (Wilheit 1986; Petty 1994a; Petty 1994b). As a result, the rainfall retrieval problem requires not only a suitable physical model but also a proper accounting for the statistical variability in the relationship between FOV-averaged rain rate and FOV-averaged microwave observables.

Bayes' Theorem states that for a given observation vector **P** (e.g., multichannel microwave observations), the posterior probability distribution of the parameter R to be estimated (e.g., rain rate) is proportional to the conditional likelihood times the prior distribution:

$$\pi(R \mid \mathbf{P}) \propto f(\mathbf{P} \mid R) \cdot \pi(R) \tag{1}$$

where $f(\mathbf{P}|R)$ is a conditional probability density function (PDF) that specifies the probability distribution of the observation **P** given parameter R. Since this distribution incorporates information concerning the physical response of the observations **P** to the parameter R (as well as the statistical variability in that response), we will refer to this part as the physical model. $\pi(R)$ summarizes our prior knowledge of the parameter before data are seen. The interaction of the physical model and the prior (e.g., climatological) probability distribution of R determines the so-called *posterior distribution* $\pi(R|\mathbf{P})$; i.e., the new PDF of R in light of the observations **P**.

Normally, the effect of **P** is to reduce the spread of $\pi(R|\mathbf{P})$ relative to $\pi(R)$; the degree of reduction is a measure of the information content of **P**.

Bayes' theorem is not an algorithm per se, but it offers a rigorous and completely general theoretical framework for retrieving atmospheric variables from remote sensing measurements. The major practical obstacle to its routine application is the need to specify the prior distribution $\pi(R)$ and conditional distribution $f(\mathbf{P}|R)$. When the parameter R is a scalar, the specification of the first of these poses no major difficulty. It is more difficult when the parameter to be retrieved is an N-dimensional vector (e.g., a hydrometeor profile), since the prior distribution is then a multivariate function that must typically be estimated from a very large ensemble of model simulations. For example, a number of papers have explicitly invoked Bayes' theorem in the design of an algorithm to infer rain rate and other rain cloud properties from multichannel microwave radiances (Evans et al. 1995; Kummerow et al. 1996, 2001; Olson et al. 1996, 2005; Bauer et al. 2001; Marzano et al. 2002; Tassa et al. 2003; Michele et al. 2005). These typically attempt to retrieve a single "best" vertical hydrometeor profile and an associated surface rain rate.

Regardless of whether R is a scalar or a vector, the accurate specification of $f(\mathbf{P}|R)$ can pose a major challenge, as it depends on accurate modeling of both the physical and statistical properties of the mapping from R to the observation vector **P**. The higher the dimensionality of both, the more difficult it is to obtain a sufficiently large and varied sample of either observations or simulations to accurately represent to conditional distribution.

Partly for this reason, we are unaware of any previous algorithm that fully exploits Bayes' theorem to explicitly provide a continuous posterior PDF of rain rate. Rather, the above algorithms are generally formulated so as to yield a single surface rain rate for each sensor field-

of-view (FOV). In the Goddard Profiling algorithm (GPROF) (Kummerow et al. 1996; Olson et al. 1996), the Bayes method is essentially reduced to a table lookup. Consequently, retrievals from GPROF are determined only by how close the observation vector is to the nearest candidates of the database, and by how often similar cloud profiles occur in the database. Furthermore, existing Bayesian retrieval algorithms depend on the representativeness of independent cloud-radiative databases and on assumptions about the form of conditional and prior likelihoods (e.g., Gaussian properties), even though training data are known to disagree with those assumptions to at least some degree.

Here we describe a new Bayesian algorithm for rain rate retrieval over the ocean using dual-polarization passive microwave images from the conically-scanning Tropical Rainfall Measuring Mission (TRMM) Microwave Imager (TMI). Unlike previous algorithms, this one is based on explicit numerical evaluation of (1). We are able to do this in part because we limit our attention to a low-dimensional problem – that of estimating a single scalar FOV-averaged rain rate R from only three microwave observables, the attenuation index $\mathbf{P}$ (defined below) at 10.65, 19.35, and 37 GHz.

This new algorithm has two unique characteristics. Unlike other Bayesian methods, ours is based on explicit mathematical models of the conditional likelihood $f(\mathbf{P}|R)$ and the prior distribution $\pi(R)$, based on empirical fits to data derived from both simulations and actual observations. Most importantly, unlike other methods, the result of our method is not a single "best" rain rate but rather a complete posterior probability distribution. A major shortcoming of existing rain rate retrieval methods has been the lack of a basis for systematically and rigorously characterizing uncertainty. Particularly in view of the highly skewed distribution of rain rates and of the non-linear response of microwave radiometers to surface rainfall, the quantification of

uncertainty is complicated by the likelihood that errors will be non-Gaussian. The lack of quantitative error information in turn hampers the optimal assimilation of rain rate estimates into models. Efforts have been made in quantifying inherent uncertainty of retrieved rain rates in GPROF (Olson et al. 2005) and the Bayesian Algorithm for Microwave-based Precipitation Retrieval (BAMPR) (Tassa et al. 2003; Michele et al. 2005) from selected cloud profiles of databases. However, the algorithm described in this paper shows that it is possible to directly applies Bayes' Theorem so that, given an observation vector from the TMI, one may obtain a complete posterior probability density function (PDF) of rain rate rather than merely a single "best" estimate of rain rate at that location.

This paper focuses on (a) the algorithm definition, (b) key aspects of the performance of the Bayesian methodology under controlled conditions; and (c) applications to TMI data. There are several components to (b). The first pertains to the performance of a Bayesian rain rate algorithm under ideal conditions – i.e., when both $f(\mathbf{P}|R)$ and $\pi(R)$ are specified perfectly. We will show that, even under such ideal conditions, systematic biases in retrieved intensity are a natural result when the physical information in the observations is insufficient to strongly constrain the results (e.g., in high rain rates, where saturation of microwave radiances tends to occur).

Since the "true" $f(\mathbf{P}|R)$ and $\pi(R)$ are normally only approximately known for real-world retrievals, the second component of our sensitivity analysis pertains to the influence of errors in the specification of these functions on the quality of the retrievals. Evans et al. (1995), using simulated data, evaluated which covariates had the greatest influence on the accuracy of retrievals. Nevertheless, their results were subject also to imperfections in the cloud model and radiative transfer model, as well as to simplifying assumptions built into both their conditional

and prior distributions. Unlike their work, we describe the results of sensitivity tests using two synthetic data sets where the "true" conditional and prior distributions are perfectly known. We are therefore able to examine the intrinsic limits in the retrievability of rain rate (based on our observables) without regard to possible errors in the models themselves.

There is the important question of how to interpret the resulting posterior rain rate PDF in terms of a single "best" rain rate for any given sensor FOV. We will show that, owing to the highly skewed properties of the posterior PDF, the choice of estimator (e.g., maximum likelihood vs. minimum variance or expectation value) is of critical importance and needs to be selected carefully with the particular application in mind. Note that the former was used in Evans et al. (1995) and referred to as the Maximum A posteriori Probability (MAP) in Marzano et al. (1999), while the latter was used in GPROF and BAMPR and referred to as minimum mean square (MMS) criterion in Tassa et al. (2003) and Michele et al. (2005).

Applications to TMI data include implements of our new Bayesian rain rate retrieval algorithm and validations against estimates from TRMM Precipitation Radar (PR). PR is an active microwave sensor that scans in a cross-track strategy from nadir to 17°. The swath width is about 215 km and the minimum detectable threshold of PR reflectivity is about 17 dBZ in the absence of attenuation. The horizontal resolution is about 4.3 km at nadir, while the vertical resolution is 0.25 km. In addition, we compare performance of our Bayesian algorithm to that of other benchmark algorithms. The algorithm may be judged successful if its overall performance at estimating surface rain rate (based on an appropriate estimator applied to the posterior PDF, such as the expectation value) is not significantly worse that that of other algorithms while also providing the detailed error information that other algorithms lack.

In the next section, we begin by reviewing the definition of the normalized polarization (or attenuation index) **P** (Petty 1994a). Because of certain desirable properties, this linear transformation of dual-polarization brightness temperatures serves as the fundamental microwave "observable" in our algorithm. In section 3, we introduce highly simplified but reasonably realistic analytic models for the local dependence of **P** on local rain rate at each frequency. The statistical variability of this relationship due to spatial averaging over realistically non-uniform rainfall is then evaluated by applying these relationships to a large set of radar-derived rain rate fields. We show that the statistical distribution of our simulated **P** in 3-space is similar to that observed in actual observations of oceanic rainfall by the TMI. Section 4 describes the construction of the prior and conditional distribution functions required by the Bayesian. The design and results of the sensitivity tests are discussed in Section 5. Section 6 presents real-world applications and validation of this Bayesian algorithm, followed by summary and discussions.

2. **TMI Attenuation Indices P**

a. Instrument description

The TMI measures dual polarized brightness temperatures at 10.65, 19.35, 37.00, and 85.50 GHz, and at 21.3 GHz with vertical polarization only. Detailed descriptions of other TMI characteristics can be found in Kummerow et al. (1998) and Bauer and Bennartz (1998). For convenience, we henceforth denote vertically polarized brightness temperatures at TMI channels as T_{10V}, T_{19V}, T_{21V}, T_{37V}, and T_{85V}, and replace V with H for horizontal polarization.

As discussed by Petty (1994a), individual channel brightness temperatures have significant shortcomings as the primary observables in a physically based rain rate retrieval

algorithm. Each channel, regardless of whether it is horizontally or vertically polarized, will respond to a variety of environmental variables, as well as to a mixture of both emission and scattering from the rain cloud itself. Petty therefore proposed the use of linear transformations of dual-polarization brightness temperatures T_V and T_H at any given frequency. These effectively decouple the emission (attenuation) and scattering contributions into two separate variables, P and S, as well as factoring out background variability due to variations in atmospheric water vapor, surface roughness, etc.

b. Definition

We limit our attention here to the attenuation index (or normalized polarization) P, which is defined as

$$P \equiv \frac{T_V - T_H}{T_{V,O} - T_{H,O}} \tag{2}$$

where T_V and T_H are the vertically and horizontally polarized brightness temperatures; $T_{V,O}$ and $T_{H,O}$ are the estimated or modeled brightness temperatures in the absence of rain or cloud. Ideally, the value of P therefore falls in the range [0,1], where 1 corresponds to a cloud-free pixel, and values approaching 0 represent a very opaque atmospheric condition generally associated with heavy precipitation.

The use of the attenuation index P in the retrieval algorithm has three advantages. First, unlike brightness temperature, it decreases monotonically with increasing rainfall intensity. Second, the attenuation index is not sensitive to the background variability because P is mainly determined by rain cloud optical thickness. Third, for the special case of a horizontally homogeneous rain layer, P and transmittance t obey an approximate power-law relationship, $P \cong t^{\alpha}$, with $\alpha \approx 1.7$. Therefore, in this limiting case, P index yields a direct indication of the

rain cloud transmittance. In this paper, our microwave observables are the attenuation indices at 10.65, 19.35, and 37.0 GHz. Our observation vector **P** is therefore given by (P_{10}, P_{19}, P_{37}).

c. Implementation for TMI

In order to convert satellite-observed brightness temperatures T_V and T_H at a given frequency to attenuation index P, we require estimates of the cloud-free background brightness temperatures $T_{V,O}$ and $T_{H,O}$. To a good approximation, these are functions of total column water vapor V and surface wind speed U. Both of these variables may be directly estimated from the passive microwave observations themselves, provided that care is taken to exclude FOVs contaminated by rain or land. The retrieved fields of V and U are then spatially interpolated into areas of precipitation and used as the basis for estimating $T_{V,O}$ and $T_{H,O}$. It is not essential that these estimates be very precise, only that they account for most of the variation in the background polarization difference $T_{V,O} - T_{H,O}$. Uncertainties in the estimate of this quantity are treated as part of the inherent observational error in P.

We derived our own empirical algorithms for V and U from match-ups between TMI radiances and surface observations. For column water vapor, we matched radiosonde observations to TMI overpasses in January and July 1999. The match-up procedure was similar to Alishouse et al. (1990) and Petty (1994b). Further details are given in Chiu (2003). The resulting statistical water vapor algorithm is given by

$$\begin{aligned} V\ [\mathrm{kg\ m^{-2}}] = {} & 128.57 + 33.94 \ln(290 - T_{19V}) \\ & -72.13 \ln(290 - T_{21V}) + 10.48 \ln(290 - T_{37H}). \end{aligned} \tag{3}$$

Match-ups between the TMI measurements and surface buoy wind data from NOAA Marine Environmental Buoy database (Chiu 2003) yielded the following algorithm for wind speed:

$$\mathrm{U\ [m\ s^{-1}]} = 130.908 + 0.170T_{10V} + 0.128T_{10H} - 0.034T_{19V}$$
$$-0.115T_{19H} - 0.079T_{21V} - 1.121T_{37V} + 0.543T_{37H}. \quad (4)$$

Empirical expressions for the background brightness temperatures were derived from 489 TMI orbits in July 1999:

$$T_{10V,O} = 154.1 + 0.076V + 0.24U + 0.47T_S$$
$$T_{10H,O} = 73.8 + 0.14V + 0.90U + 0.24T_S$$
$$\ln(300 - T_{19V,O}) = 4.89 - 0.0072V - 0.0017U - 0.0025T_S$$
$$\ln(300 - T_{19H,O}) = 5.39 - 0.0078V - 0.0063U - 0.00052T_S$$
$$\ln(300 - T_{37V,O}) = 4.65 - 0.0058V + 0.00055U - 0.00069T_S$$
$$\ln(300 - T_{37H,O}) = 5.22 - 0.0065V - 0.0080U + 0.00031T_S, \quad (5)$$

where V and U were estimated by (3) and (4), and sea surface temperature T_S (°C) was obtained from a climatological database (obtained from NASA/GSFC).

3. **Radar-radiative simulations**

a. Simulated P for realistic rain fields

A key part of our algorithm is the specification of $f(\mathbf{P} \mid R)$, which depends on both the physical and statistical properties of rainfall, especially the variable effects of beam-filling, which we take to be the single most factor determining the normalized polarization (this is not true for the single-channel brightness temperatures). Since actual match-up data from microwave and rainfall measurements or detailed model simulations do not exist in a sufficient quantity, we rely on simulated data derived from high-resolution radar composites.

1) RADAR DATA

As previously mentioned, beam-filling errors due to inhomogeneities of rain clouds result in a non-unique relationship between rain rate and microwave signal, and these contribute to significant ambiguities in passive microwave retrievals. In order to account for rain cloud inhomogeneity in our specification of $f(\mathbf{P} \mid R)$, we used NWS WSR-88D radar operational reflectivity data to obtain spatially realistically rain rate fields for use in simple radiative transfer simulations designed to capture the contribution of horizontal inhomogeneity to fluctuations in the P–R relationship for any given frequency.

The reflectivity data were operational gridded composites of 154 NWS WSR-88D sites in the US with an hourly temporal resolution and a spatial resolution of 1 km. Reflectivity values were converted to rain rate using the Marshall and Palmer (1948) relationship $Z = 200R^{1.6}$. (This relationship is intended only to yield statistically reasonable spatial patterns of rain intensity for use in the simulations, not absolutely calibrated rain rate estimates.) A total of 22 radar reflectivity files were randomly selected during July and August 2002, each comprising an average of 3×10^4 rainy pixels. Because of the coarseness of the digitization of reflectivity Z, small upward and downward shifts in Z were applied to each image in order to yield a reasonably smooth combined histogram of modeled rain rates. This procedure effectively multiplied the number of radar grids to 110. The reader is referred to Chiu (2003) for additional details.

2) POLARIZATION CALCULATIONS

Starting with the precipitation structures simulated from the radar measurements, we simulated satellite-observed polarization P via a simplified plane-parallel radiative transfer model. The mass extinction coefficient of suspended cloud water $\kappa_{e,l}$ is listed in Table 1, which

where the simulated brightness temperature $T_{B,p}$ at polarization p (vertical or horizontal) is determined by the transmittance t, the specular emissivity of the surface (sea water in the study) ε_p, the surface temperature T_S, and the air temperature T_A. The transmittance t is given by

$$t = \exp\left[-\frac{\tau}{\cos\theta}\right], \tag{10}$$

where θ is the incidence angle and τ is the total optical depth due to hydrometeors. The surface temperature was approximated from the extrapolation of the temperature profile, assuming a temperature at the freezing level of 0°C and a lapse rate of 6.5 K/km. T_A was estimated by the air temperature at the mid point between the surface and Z_f. Since the emissivity of the ocean is polarized, both the vertically and horizontally polarized radiance was obtained.

We define t_a, t_l, and t_r as the transmittance attributed to the atmosphere, the suspended cloud water, and the rain water, respectively, and t_1 as the total transmittance (the product t_a, t_l, and t_r). Based on (2) and (9), it can be shown that the attenuation index (normalized polarization) can be written as

$$P = \frac{t_1\left(T_S - T_A\right) + t_1^2 T_A}{t_a\left(T_S - T_{A,O}\right) + t_a^2 T_{A,O}}, \tag{11}$$

where $T_{A,O}$ represents the air temperature when the suspended cloud water and rain water are absent. We assume $T_A \approx T_{A,O}$ in the simulations. In addition, the order of the first term for both the numerator and denominator is much smaller than the second term. Therefore, the attenuation index can be approximated as

$$P \approx \left(\frac{t_1}{t_a}\right)^2 = \left(\frac{t_a t_l t_r}{t_a}\right)^2 = t_l^2 t_r^2, \tag{12}$$

was computed from Liebe et al. (1991) assuming a temperature of 0°C. The relationship between the volume extinction coefficients of rain water $k_{e,r}$ and rain rates (R) was estimated from Mie theory, assuming spherical rain drops with a liquid water temperature of 10°C and Marshall-Palmer drop size distribution. A power-law form was found to approximate the relationship well (Petty 1994b),

$$k_{e,r} = aR^b, \tag{6}$$

where coefficients a and b for each channel are shown in Table 1. The rain layer optical depth τ_r was then modeled as

$$\tau_r \cong Z_f k_{e,r}(R), \tag{7}$$

representing the contribution of suspended rain water to attenuation of the polarized ocean surface emission. Since there was no information about the values of the freezing height Z_f in the radar reflectivity product, a fixed value of 3 km was assumed for the purposes of this demonstration. The optical depth τ_l attributed to suspended cloud water was modeled as

$$\tau_l = \kappa_{e,l} L, \tag{8}$$

where variations in the suspended cloud water content (L in kg/m^2) were simulated via a lognormal random deviate applied to each grid cell.

Because depolarization of the ocean surface emission by rain clouds depends primarily on total path attenuation and not on the details of the vertical structure of temperature or hydrometeor properties, we may use a highly simplified 1-D plane-parallel model to compute brightness temperatures at each grid point. The radiative transfer equation is written as

$$T_{B,p} = (1-t)T_A + \varepsilon_p t T_S + (1-t)(1-\varepsilon_p) t T_A, \tag{9}$$

Three important characteristics of **P** are shown in Fig. 1. First, theoretically, in a homogeneous case of rain cloud, a unique non-linear relationship in **P** is expected. However, in reality, due mainly to variable beam-filling, **P** exhibits considerable scatter in 3-D space. Both observations and simulations show similar magnitudes of this effect. Second, P may sometimes be slightly greater than 1 in cloud-free cases (but smaller than 1.1 in most cases), due to a combination of instrument noise, errors in water vapor and surface wind speeds, and errors in regression equations. Our analytic models for the conditional distribution will account for this effect. Third, polarization differences at 10.65 GHz of less than 30 K are exceedingly rare in the TMI data set; correspondingly, very few observed values of P_{10} are less than 0.4. This observation highlights the fact that rainfall is almost never both horizontally uniform and heavy enough to saturate the 10.65 GHz channel.

4. Algorithm basis

As stated in Bayes' theorem, the Bayesian posterior density function is determined by conditional likelihoods that statistically describe physical relationships between rain rate and microwave signal, and a prior rain rate distribution that represents our knowledge. Therefore, there are three key elements in our algorithm: the conditional likelihood, the prior distribution, and the estimator interpreting the posterior distribution. In this section, we introduce generic forms to model the prior and conditional distributions. These forms fitting to radar-radiative model simulations will be a basis for further sensitivity tests.

a. Conditional probability density function

Note that t_a cancels out in the calculation of P, and thus the absolute value of t_a has little effect on P. Therefore, cloud-free brightness temperatures can be easily approximated employing a transmittance of unity in (9), in which case $T_{B,O} = \varepsilon T_S$.

Once the high-resolution field of P had been computed for each simulated rain rate field, both the rain rate field and the P field were spatially averaged. The rain rate field was averaged using a moving window of 15×15 km, representing the nominal retrieval resolution of the algorithm. The simulated P values for each TMI channel were spatially averaged using a Gaussian approximation to the effective field-of-view for that channel. Gaussian random noise with standard deviations of 0.01, 0.02, and 0.02 for 10.65, 19.35, and 37.00 GHz channel, respectively, was then added to **P** in order to reasonably account for errors due to the highly simplified nature of the forward model, instrument noise, and similar variables. The above procedure yielded a large ensemble of matched FOV-averaged rain rates R and attenuation indices P_{10}, P_{19}, and P_{37}.

3) COMPARISIONS WITH TMI-DERIVED ATTENUATION INDEX

To evaluate the statistical representativeness of our simulated **P**, we compared the 3-D PDF of **P** derived from the simulations with that obtained from 110 actual TMI orbits during 1999 and 2000 were obtained. Fig. 1 compares 2-D slices from the 3-D distributions for simulated and actual data. Despite the simplicity of the forward model and the utilization of continental radar observations as a proxy for the spatial structure of oceanic rainfall, there is surprisingly strongly qualitative similarity between the two distributions. We can therefore have some confidence in the utility of our simulations for constructing our Bayesian algorithm and for conducting further sensitivity tests.

The conditional likelihood $f(\mathbf{P} \mid R)$ is a multivariate probability distribution. We used two methods to characterize the conditional PDF. The first method is to use a covariance matrix to include linear relationships only between rain rate and microwave signature, which is similar to the parameterization of current available Bayesian algorithms. However, as shown in observations and simulations (Fig. 1), linear properties are not sufficient to approximate the multichannel dependency of microwave signature. Therefore, in the second method, we took a successive approach to describe the conditional PDF that included linear as well as non-linear relationships. We will refer to these as "the linear model" and "the nonlinear model", respectively.

1) THE LINEAR MODEL

Similar to a multivariate Gaussian distribution, the conditional PDF between **P** and R can be written as

$$f(\mathbf{P} \mid R) \propto P_{10}(a - P_{10}) P_{19}(a - P_{19}) P_{37}(a - P_{37}) \exp\left[-\frac{1}{2}(\mathbf{P} - \boldsymbol{\mu}) C^{-1} (\mathbf{P} - \boldsymbol{\mu})^T\right]. \quad (13)$$

This closed-form function is essentially a normal distribution in the interior of the interval [0, a] but is forced to zero at the boundaries by the term of $P(a- P)$ for each frequency. a is chosen to be 1.1, based on observed ranges of actual TMI-derived values. C is the covariance matrix, and $\boldsymbol{\mu}$ is

$$\boldsymbol{\mu} = (\mu_1, \mu_2, \mu_3); \quad (14)$$

$$\mu_i = a_{\mu,i} \exp\left[-b_{\mu,i} R\right] + c_{\mu,i}, \quad (15)$$

where the subscripts 1, 2, and 3 describe the quantities at 10.65, 19.35, and 37.00 GHz, respectively. Subindex i is the corresponding channel. Based on the radar-radiative simulations, there parameters can be approximated by Table 2 and

$$C = \begin{bmatrix} 0.010 & 0.015 & 0.020 \\ 0.015 & 0.040 & 0.045 \\ 0.020 & 0.045 & 0.060 \end{bmatrix}. \tag{16}$$

2) THE NONLINEAR MODEL

The more complete physical model is developed to account for the linear as well as non-linear relations of **P** to rain rate. The distribution of **P** at a given rain rate R is approached hierarchically:

$$f(\mathbf{P} \mid R) = f(P_{37} \mid R) f(P_{19} \mid P_{37}, R) f(P_{10} \mid P_{19}, P_{37}, R), \tag{17}$$

where $f(P_{37} \mid R)$ is the likelihood of P_{37} at a given R; $f(P_{19} \mid P_{37}, R)$ is the PDF of P_{19} when P_{37} and R are fixed; and the $f(P_{10} \mid P_{19}, P_{37}, R)$ describes the PDF of P_{10} while the other three variables are known. These conditional PDFs, for example, can be approximated as

$$f(P_{37} \mid R) \propto P_{37}(a - P_{37}) \exp\left[-\frac{1}{2\sigma_3^2}(P_{37} - \mu_3)^2 \right]; P_{37} \in [0, a], \tag{18}$$

$$f(P_{19} \mid P_{37}, R) \propto P_{19}(a - P_{19}) \exp\left[-\frac{1}{2\sigma_2^2}(P_{19} - \mu_2)^2 \right]; P_{19} \in [0, a], \tag{19}$$

where μ_2, μ_3, σ_2 and σ_3 are all determined by fitting the same radar-radiative model simulations. Complete parameterizations can be found in Chiu (2003).

b. The prior distribution of rain rate

Surface rain rate distributions have been commonly parameterized by lognormal functions (Houze and Cheng 1977; Kedem and Chiu 1987; Kedem et al. 1990, 1997; Sauvageot 1994; Nzeukou and Sauvageot 2002), although some observations showed departures from the lognormal distribution (Jameson and Kostinski 1999) and some suggested that rain rates followed gamma distributions (Ison et al. 1971; Swift and Schreuder 1981; Wilks and Eggleston

1992). Since Cho et al. (2004) found that both lognormal and gamma distributions were able to characterize the PDF of rain rates from TRMM data, we used lognormal functions as the prior distribution.

The lognormal density function for the prior distribution is denoted as $\log N(\mu,\sigma)$ and defined as

$$\log N(r \mid \mu,\sigma) = \begin{cases} \dfrac{1}{R\sigma\sqrt{2\pi}} \exp\left[-\dfrac{1}{2\sigma^2}(\ln R-\mu)^2\right], R>0 \\ 0, R=0 \end{cases} \tag{20}$$

where μ and σ are the mean and standard deviation (mm/hr) of the variable. These two parameters vary with different rain rate observation datasets. Therefore, we will evaluate the effect of varying (μ, σ) on the simulated retrievals.

c. Estimators of the posterior distribution

When the conditional and prior likelihoods are specified, based on the Bayes' theorem ((1)), the posterior distribution can be derived by

$$\pi(R \mid \mathbf{P}) = \frac{f(\mathbf{P} \mid R)\pi(R)}{\int f(\mathbf{P} \mid R)\pi(R)dR}. \tag{21}$$

Integrations with respect to rain rate in the four-dimensional space were performed numerically. Once the posterior distribution is known, the two most common estimators were taken: the mean and the maximum likelihood estimate of the posterior probability distribution, denoted as MEAN and MLE, respectively. The corresponding Bayesian estimates are stored in a 3-dimensional lookup table for each **P** for single-pixel retrievals.

5. Sensitivity tests

a. Experiment design

A number of experiments are designed for the sensitivity test by various combinations of the prior and conditional likelihoods (summarized in table 3). The retrieval target was produced from a random number generator that followed all conditional PDFs of the nonlinear model ((17)–(19)). Since one of our purposes for the sensitivity tests is to better understand the behavior of retrieval at higher rain rates, we generated this dataset along with the prior distribution log$N(0, 2)$ to prevent a scarcity of high rain intensity.

Control run (R0) is the experiment that the Bayesian retrieval method uses exactly same conditional and prior PDFs with the retrieval target. An analysis of this control experiment can provide insight into the inherent uncertainty of the retrieval, since each PDF is perfect and no assumption is made in the algorithm. Furthermore, by comparing the control run with other experiments, the sensitivity of the algorithm to the prior distributions of rain rate can be evaluated by experiments R1 and R2, while R3 and R4 aim to understand the sensitivity to the conditional likelihoods. In experiment R3, we used a different parameterization for $f\left(P_{19} \mid P_{37}, R\right)$ to investigate the sensitivity of the algorithm to various explicit functions. Experiment R4 applies the **P**–R relationships of the linear model (i.e., covariance matrix form) into the algorithm. This experiment is vital because it evaluates the adequacy of simple assumptions of the conditional PDFs in the retrieval algorithm, when in fact the dataset has a much larger degree of complexities.

b. Intrinsic uncertainty of the algorithm

As we have emphasized through this paper, a key property of the Bayesian algorithm is its ability to obtain complete posterior PDFs of retrieved rain rates. Based on the complete posterior distribution, a probability statement can be made about the realization of the retrieval. This advantage allows us to assess intrinsic uncertainties of the retrieval, when the ideal physical model and exact prior distribution are applied to the algorithm.

Figure 2 shows examples of the posterior distributions from experiment R0. Some posterior distributions have a single maximum over the entire rain rate range, but some have two. A single maximum expresses the situation that a given observation vector **P** provides unambiguous information about the most likely rain rate when both physical relationships and prior knowledge are taken into account. A bimodal distribution implies that two distinct rain intensities are of comparable likelihood. The peak on the left indicates a scene of widespread stratiform precipitation associated with a smaller rain rate, while the second peak suggests the possibility of a strong convective cell within that 15×15 km area. Based on the posterior PDFs of Fig. 2b, the MLE retrieval can increase from 5 to 60 mm/hr if P_{10} decreases from 0.64 to 0.60 and P_{19} and P_{37} remain the same. However, in reality, this magnitude of the change in P value may not relate to a dramatic change of rain intensity of the scene, but rather arises from the variations of the instrument noise, atmospheric condition, or/and the calculations of brightness temperatures. Therefore, caution should be exercised in these cases when single-pixel retrievals are of interest. Such cases may be easily detected via their larger associated standard deviations.

Performance of the Bayesian algorithm at different rain rate ranges for R0 experiment is demonstrated from the histogram of retrieved rain rates (as shown in Fig. 3). The title for each subplot is made of three components. The first component, RR, indicates the specific range of rain rates, where the retrieved rain intensity is drawn if its corresponding true rain rate in the

training dataset is in this range. The second component is the sample size of the histogram. The third component, MEAN or MLE, describes the estimate used to interpret the posterior distribution. The pair of the numbers on the upper-right corner in each subplot are the mean and standard deviation of the histogram, while the percentage is the proportion that the retrieved rain rates are in the same range as the actual rainfall intensities with respect to the whole histogram. Note that for the true range RR lower than 30 mm/hr, the histogram is plotted in a logarithmic scale.

Results from R0 experiment using MEAN estimates suggest that the Bayesian algorithm is able to retrieve the light rain rate very well. For the moderate intensity (7–15 mm/hr), the retrieval algorithm captures 46% data points, and the mean value is about right. The algorithm tends to underestimate the rain rates when the actual intensity in training data increases to a heavier range. Meanwhile, the associated standard deviation of the histogram starts to increase as well. Even so, the retrievals still encompass 30% data in the true range. For the extremely large rain rate (greater than 75 mm/hr), there are 42% of data in the correct rain range, and the mode of the histogram falls within the true range. In this control experiment, the Bayesian algorithm shows the ability to retrieve rain intensity over all ranges, even for the case with extremely heavy precipitation.

The histogram of MLE retrievals for experiment R0 is shown in Fig. 4. Results from the light rain regime demonstrate a satisfactory performance. However, the underestimation for intermediate intensities (4 to 30 mm/hr) is significant. Moreover, there are two distinct modes in the histogram when the true range RR goes up greater than 30 mm/hr. The one associated with a lower rainfall rate dominates in the RR range of [30, 75] mm/hr, and causes some retrievals at

least 20 mm/hr smaller than the true rain intensity. The other mode becomes dominant under the extremely heavy precipitation, yielding 40% data points in the correct range.

In short, R0 experiment has demonstrated the retrieval ability of the Bayesian algorithm over various rain rate ranges when the prior and conditional likelihoods are both idealized. The single-pixel retrieved rain rates might be associated with a bias due to the inherent uncertainty in the physical relationships and the interpretation using MEAN and MLE. The inherent uncertainty might be reduced via the inclusion of additional information concerning other atmospheric or microwave variables.

c. Sensitivity to the prior knowledge

Analyses of experiments R1 and R2 demonstrate how retrieved rain rates change to various specifications of the prior distribution when the physical model remains the same. Compared to the control prior density function, the prior distribution in R1 experiment, $\log N(0,1)$, has relatively smaller probabilities at very light rain rates and beyond 5 mm/hr. This property of the prior PDF leads the algorithm to retrieve reasonably for the true intensities between 0.2 and 7 mm/hr from both MEAN and MLE estimates. However, the smaller probability of the prior PDF at higher rain rates obviously limits the ability of the algorithm to retrieve heavy precipitation as shown in Fig. 5. Note that we also conducted other experiments changing μ and σ by 10% in prior PDFs, and found that slight variations of the prior distribution had no significant effects on the Bayesian algorithm.

A non-informative prior distribution is used in experiment R2, which assigns equal weight to all values over the parameter space. Based on the Bayes' theorem, it is clear that the posterior probability density is now proportional to the likelihood represented only by the data in

this experiment, and thus the retrieval is dominated by the behavior of the physical model. Results demonstrate that a uniform prior PDF yields much higher retrieved rain rates by 7–15 mm/hr in light and moderate rain situations (not shown). For the true range with heavier rain rates, experiment R2 captures around 50% data points in the correct range. Since experiment R2 only includes the information of data with no prior knowledge, it is suggested that the **P** we used is sufficient to reflect the rainfall signal even in heavy precipitating systems.

In summary, the prior rain rate distribution plays a crucial role in the Bayesian algorithm retrieval, since the characteristics of the prior PDFs determine the retrieval ability and bias at different rain rate ranges. However, the Bayesian retrieval is not sensitive to slight fluctuations of the parameters used in the prior PDFs. Therefore, when the prior rain rate distribution is applied reasonably, the Bayesian algorithm is still robust.

d. Sensitivity to the conditional distribution

This section advances our understanding of the sensitivity of Bayesian retrievals to the characterization of conditional likelihoods that provide statistical and physical relationships between **P** and R. First, we attempted to understand whether different explicit functions characterizing conditional distributions would have a substantial impact on retrievals. In experiments R0 and R3, the conditional PDFs were both derived from the same radar-radiative simulations, and they presented very similar relationships between **P** and R. As a result, experiment R3 yields very consistent retrievals with R0 experiment for both MEAN and MLE estimates (not shown). It indicates that the specifications of the conditional distributions are not critical if the P–R relationships represented by those PDFs are not far from reality.

Second, we attempted to evaluate the adequacy of using simplified conditional PDFs to represent more complicated behaviors of data by experiment R4. Fig. 6 depicts the microwave multichannel relationships represented in the experiment R0 (upper panel) and R4 (bottom panel). These relationships demonstrate similar patterns, including the orientation and spread-out of the contours. However apparently, the locations of the maximum likelihoods are shifted to lower P values in experiment R4.

Histograms of retrievals from the MEAN estimates of experiment R4 are shown in Fig. 7 (results of MLE are not shown due to similar responses). In general, for both MEAN and MLE estimates, the use of a linear covariance matrix to describe conditional likelihoods significantly overestimates rain rates, and the variations of the retrieval histograms are almost twice than those of the control experiment R0. More specifically, for very light rain rates, R4 only produces 0.1% data points in correct ranges, while the control run successfully retrieves almost half of data. The positive bias becomes more significant when true rain rates are with moderate intensity. Under the condition that the true rain rates are only 2 to 15 mm/hr, some retrieval from R4 are even greater than 50 mm/hr. The large variation in retrieved intensity is also seen in the case of heavy precipitation.

One should not conclude that a simplified physical model is always unsuitable for the use of a Bayesian algorithm, since considerable differences exist in the multichannel relationships between the retrieval target dataset and the applied physical model for experiment R4. The retrieval bias may be reduced if the simple physical model is improved or tuned to be closer to the training dataset. However, we must note that the covariance matrix facilitating the linear model was estimated from the same radar-radiative simulations that were used in the explicit

functional model. Therefore, it is clear that the simplified physical model cannot explain all of data behaviors, and this deficiency will lead to a significant bias in some ranges of rain rates.

6. Applications to TMI data

This section provides applications of our new Bayesian algorithm to TMI data, including implements and validations against PR data. In previous sections, we trained our algorithm with radar-radiative simulations. In an attempt to construct an algorithm based on calibrate precipitation measurements, we used the same framework here, but the prior and conditional PDFs were adjusted based on actual PR and TMI match-ups.

a. PR-TMI match-up data

Since there is no long-term/wide-area dense rain gauge network or other reliable data to provide true rainfall intensity over the ocean, we used near-surface rain rates of TRMM standard product 2A25 (retrieval from the Precipitation Radar (PR)) to develop and validate our TMI Bayesian retrieval algorithm. The 2A25 PR products provide retrieved rain rates with 4-km resolution. Since our retrievals represented rain intensity at a 15-km resolution, PR surface rain rates were averaged using a Gaussian weighting function and interpolated to the locations of TMI pixels. For convenience, the averaged rain rate estimates are hereafter referred to as PR rain rates. Note that PR reflectivity measurements can suffer from sidelobe contamination when the main beam of the PR is off-nadir, and the resulting errors would propagate into rain rate estimates. To minimize the likely impact of these errors, only match-ups between TMI observations and near-nadir PR estimates are utilized.

The probability distribution of near-nadir 15×15 km PR rain rates from data of January, April, July, and October 1998 was found to be comparable with (20). Due to the minimum detectable threshold (~17 dBZ) of PR reflectivity, we applied a cut-off of 0.04 mm/hr to yield parameters (μ, σ) of (−2.8, 2.0). In addition, we used two months PR–TMI match-ups (January and July, 1998) to adjust conditional PDFs of our Bayesian algorithms. Detailed parameterizations are given in Chiu (2003).

b. Validation datasets

We used a number of cases to evaluate overall performances for all algorithms. In addition to looking at quasi-global performance, we also considered specific classes of precipitating systems. These included tropical cyclones, frontal rain bands in extra-tropical cyclones, and some scattered strong convection cells. The purpose behind the selection of these cases is to evaluate the degree to which algorithm performance depends on the nature of the precipitation cloud system under consideration, especially when the latter is in some sense atypical of global precipitation.

1) INDIVIDUAL TEST CASES

A typhoon case from TMI orbit number 336 as well as twelve oceanic cases from Bauer et al. (2001) were selected as individual test cases for retrieved rain rates. As before, the "true" rain rate in the validation dataset is obtained from the coincident PR 15×15 km averaged rain rate.

2) 1998/04 PR-TMI GLOBAL MATCH-UP DATA

For quasi-global validation purposes, 118 orbit files in April 1998 were randomly selected to validate the overall performance of all algorithms. Note that our Bayesian retrieval

algorithm was derived from the data of January and July in 1998, and therefore, the PR–TMI match-up data of April is independent for the purposes of this validation.

c. Benchmark algorithms

Two benchmark algorithms are utilized in this study to provide intercomparisons for the purpose of validations. One benchmark algorithm is the Goddard Profiling algorithm (GPROF), which is the official algorithm for TMI data (Kummerow et al. 1996, 2001; Olson et al. 1996, 2005). This algorithm introduced a database to represent the presumed probability distribution of rain rate and cloud profiles. Cloud profiles with microwave signatures that are close to satellite observations are picked from the database as candidates. The selected candidates are then averaged to yield the best surface rain rate and precipitation structure for each pixel, based on the relative occurrence of each cloud profile in the database.

The other benchmark algorithm is a linear regression model developed from PR–TMI match-up data in January and July 1998. Regression variables include the P_{10}, P_{19}, P_{37}, and scatter index at 37 and 85 GHz (S_{37}, and S_{85}, Petty 1994a). The linear model is formulated as follows:

$$
\begin{aligned}
P_{10}^{*} &= \frac{P_{10}^{\lambda_1} - 1}{\lambda_1}, \lambda_1 = -0.8 \\
P_{19}^{*} &= \frac{P_{19}^{\lambda_2} - 1}{\lambda_2}, \lambda_2 = -0.3 \\
P_{37}^{*} &= \frac{P_{37}^{\lambda_3} - 1}{\lambda_3}, \lambda_3 = -0.7
\end{aligned}
\tag{22}
$$

$$
\begin{aligned}
R = {} & 0.201 + 4.10P_{10}^{*} - 4.831P_{19}^{*} + 0.182P_{37}^{*} + 0.110S_{37} + 0.017S_{85} \\
& + 0.810P_{10}^{*}P_{19}^{*} + 0.960P_{10}^{*}P_{37}^{*} - 0.234P_{19}^{*}P_{37}^{*} + 0.117P_{10}^{*}P_{19}^{*}P_{37}^{*},
\end{aligned}
$$

where R is retrieved rain rate in mm/hr, and the asterisk symbol represents transformed variables. In this model, all pixels were retrieved without rain screening. Therefore, some constraints were needed for calculated rain rate fields in order to exclude unrealistic precipitation. It is assumed that the pixel is not rainy when its retrieved rain intensity is smaller than 0.5 mm/hr.

The linear algorithm may be regarded as the least sophisticated of the algorithms, in that it does not account for either nonlinearity in the relationship between R and the microwave observables or the highly non-Gaussian distributions of these variables. Hence, differences in the performance of this algorithm from the other algorithms may be regarded as a measure of the relative importance of these characteristics.

d. Validation metrics

There are several common validation statistics employed to characterize differences between retrieved estimates and true values. Of these, the difference between the means (or mean bias, henceforth BIAS), the root-mean-squared difference (henceforth RMSD), and the linear correlation coefficient are the most commonly used. It bears emphasizing that no performance statistic for any single algorithm is meaningful when considered in isolation, as it invariable depends on the statistical and physical properties of the validation data set. We can therefore assess the "goodness" of any outcome only by comparing the results of several competing algorithms applied to identical data sets.

The linear correlation coefficient represents the strength of the linear relationship between observations and retrievals. Unlike either BIAS or RMSD, it is not affected by linear systematic errors in either the validation data or the retrievals and it is therefore a better measure of intrinsic (or potential) algorithm performance at discriminating between high and low rain

rates. However, a systematic *non*-linear bias, though potentially correctible, will adversely affect the correlation coefficient and therefore give a misleading indication of intrinsic algorithm skill.

A drawback to any of the traditional metrics is that they do not distinguish between performances at high and low rain rate values; moreover, they do not necessarily distinguish between systematic errors due to correctable nonlinearities in an algorithm's response and retrieval errors of a more random (and therefore non-correctable) nature. We therefore also employ an adaptation of the Heidke Skill Score (HSS) proposed by Conner and Petty (1998). They specified separate rain rate thresholds R_v and R_r for the validation data and for the retrievals, respectively, and to allow these to vary independently of one another. The HSS may then be computed and plotted as a continuous bivariate function of the two thresholds. One may then identify those combinations of the two thresholds that maximize the skill score. *The maximum skill found for any given value of R_v is independent of any calibration bias (linear or non-linear) in the retrievals.* This method therefore offers a way of characterizing the intrinsic performance of an algorithm at discriminating between high and low (or zero) rain rates, independent of any biases, while also allowing the presence of any such biases to be inferred via the relationship between R_v and R_r that maximizes the skill score.

e. Results

The performance of all algorithms as measured using conventional validation statistics (bias, root-mean-squared error, and correlation coefficient) are summarized in Table 4. For the purposes of this study, the outcome is deemed satisfactory if the performance of our Bayesian algorithm is found to be comparable to that of other algorithms, given that ours has the added advantage of producing posterior PDFs of surface rain rates.

1) TYPHOON CASE

Table 4 shows that the Bayesian-MEAN has a zero bias, a comparable correlation coefficient with GPROF and the linear model, and a slightly larger RMSD for TMI orbit 336. To obtain a direct sense of how different the retrieval from each algorithm behaves, PR and algorithm-retrieved rain rates are mapped in Fig. 8. Qualitatively, all algorithms are able to retrieve the eye, two separate rain bands, and the overall cyclonic structure of the typhoon. Quantitatively, most algorithms produce rain rate intensities of similar magnitude to the PR interpolated data. A scatter plot of retrieval vs. PR rain rate (Fig. 9) also demonstrates good agreements for all algorithms, though underestimations are seen when rain rates exceed 30 mm/hr. In addition, the dynamic retrieval range in the Bayesian-MLE algorithm is around 10 mm/hr in this case, which is much smaller than that derived from the posterior mean. This deficiency leads to a significant negative bias in Bayesian-MLE retrievals (Table 4).

Figure 10 illustrates posterior PDFs for points A–D that are marked in Fig 8d. Point A is located around the eye of the typhoon, and has a narrow spectrum and distinct peak at a smaller rain rate. Points B and C are on the different sides of the wall. Their PDFs show that Point B has a heavier tail and thus yields a much larger mean rain rate than Point C. Point D is located in the one of spiral rain bands. Its associated posterior PDF has a heavy tail as well, and highly skewed to the right.

2) BAUER'S 12 OCEANIC CASES

For these twelve oceanic cases, retrievals from the Bayesian-MEAN algorithm associate with a bias of only 0.08 mm/hr (Table 4), but have a larger root-mean-squared error and a

smaller correlation coefficient, implying the lack of retrieval ability for heavy rain rates. The linear model has zero bias and the largest correlation coefficient here. The Bayesian-MLE has comparable performance with GPORF for these cases.

Figure 11 shows contours of 2-dimensional HSS of each algorithm, and indicates that the highest skill scores occur in the range of 0-10 mm/hr for all algorithms. For any given validation rain rate threshold R_v, the value of the algorithm rain rate threshold R_r can be identified for which the HSS is maximized. We may refer to this as the optimized rain rate threshold R_{opt} for that value of R_v. Two additional useful types of plots follow from this definition. One is a plot of the R_{opt} vs. R_v, which is indicative of apparent bias, relative to the validation data. The other is the plot of maximum HSS (i.e., the skill score computed at R_{opt}) vs. R_v, which represents the intrinsic (bias-independent) discrimination ability of the algorithm with respect to rain rates exceeding R_v.

Figure 12 depicts the relationship between R_{opt} and R_v for the ensemble of twelve overpasses. The linear relations revealed in plots demonstrate that most algorithms, especially the Bayesian-MEAN model, offer good agreement with PR data when true rain rates is less than 20 mm/hr. The degradation at higher rain rate in our Bayesian algorithm originates from insufficient data samples at higher rain rate, and the resulting poor fit to the data when we specified our conditional likelihoods. Fig. 13 shows the maximum Heidke skill score vs. R_v for this data set, and all algorithms have comparable discrimination abilities. Since the proportion of number of hits to the total data points in the contingency table for all algorithms drops dramatically (to less than 1%), the maximum HSS might not be statistically meaningful when true rain rate is above 10 mm/hr. Therefore, we only show the maximum HSS for rain rates up to 10 mm/hr.

3) APRIL 1998

In the randomly selected cases in April 1998, our Bayesian retrieval algorithms show the smallest bias and a comparable correlation coefficient with that of GPROF. The linear model has the best correlation with PR, but is associated with a negative bias. HSS analysis reveals satisfactory performance of our Bayesian algorithms (figures not shown).

7. Summary and discussions

This paper has introduced a new Bayesian retrieval algorithm that provides continuous posterior probability distributions of rain rate from satellite microwave observations. The generic forms of this algorithm were comprised of explicit, closed-form functions, and based on simulations using high-resolution radar composites and 1D plane-parallel radiative transfer model. From the derived posterior distributions, various statistical estimators, such as the mean and maximum likelihood estimate, can be used to serve as the single-pixel retrieved rain rate, depending on the desired characteristics of the retrieval purpose.

We used synthetic randomly-generated datasets to clarify the theoretical advantage of the Bayesian algorithm, as well as to demonstrate its retrieval ability when imperfect information was applied to the algorithm, which is often the case in reality. We should be aware of the inherent retrieval uncertainty associated with certain scenes, especially in connection with variable beam-filling effects. In addition, a significant low bias at higher rain rate is found even when the prior and conditional likelihoods are perfectly modeled. This bias is attributed to the loss of physically direct information concerning rain rate due to saturation of microwave observables. In such cases, the prior PDF supplies most of the information to the posterior PDF and favors the more frequent lesser rain rates.

The sensitivity tests revealed that retrieved surface rain rate is sensitive to assumptions in the prior rain rate distribution. The effect of the prior distribution on retrieval is different at various rain rate ranges, mainly determined by the characteristics of the prior PDF. We also found that a simple covariance matrix is not sufficient to describe statistical and physical dependency of microwave measurements on rain rate. This insufficiency can lead to substantial errors and bias in retrieval. On the other hand, a use of explicit functional models can provide more accurate and complete relationships without increasing computational loading. Once these explicit, closed-form functions are well fitted to the training dataset, the Bayesian algorithm is not very sensitive to the slight change in the parameterizations.

Applications to TMI data demonstrate that the performance of our Bayesian algorithm is comparable with that of GPROF and a new linear model, while ours also provides complete posterior rain rate probability distributions. In general, retrievals from the Bayesian-MEAN algorithm have very small biases and good linear correlations with PR-derived rain rates. The Bayesian-MLE algorithm revealed an excellent ability to retrieve light rain intensity (shown in sensitivity tests as well). However, the maximum-likelihood rain rate is generally much less than the expectation value obtained from the same posterior PDF, especially for higher rain rates. If unbiased averages over time and/or space are required, then the Bayesian-MEAN algorithm is the preferred choice. But if more representative rain rates in areas of light rain are required in instantaneous ``snapshots" of precipitating systems, the Bayesian-MLE result might be preferred.

We also found that our Bayesian algorithms had greater difficulty retrieving the heaviest rain rates. Large errors in retrieving heavy rain rates, even though the latter are relatively infrequent, can have large effects on computed root-mean-square errors and correlation coefficients. The inability of all algorithms to achieve unbiased results in heavy rainfall is partly

Houze, R. A. and C.-P. Cheng, 1977: Radar characteristics of tropical convection observed during GATE: mean properties and trends over the summer season. *Mon. Wea. Rev.*, **105**, 964–980.

Ison, N. T., A. M. Feyerherm, and L. D. Bark, 1971: Wet period precipitation and the gamma distribution. *J. Appl. Meteor.*, **10**, 658–665.

Jameson, A. R., and A. B. Kostinski, 1999: Fluctuation properties of precipitation. Part V: Distribution of rain rates – Theory and observations in clustered rain. *J. Atmos. Sci.*, **56**, 3920–3932.

Kedem, B. and L. S. Chiu, 1987: Are rain rate processes self-similar? *Water Resour. Res.*, **23**, 1816–1818.

– –, L. S. Chiu and G. R. North, 1990: Estimation of mean rain rate: application to satellite observations. *J. Geophys. Res.*, **95**, 1965–1972.

– –, R. Pfeiffer, and D. A. Short, 1997: Variability of space–time mean rain rate. *J. Appl. Meteor.*, **36**, 443–451.

Kummerow, C., W. Barnes, T. Kozu, J. Shiue and J. Simpson, 1998: The tropical rainfall measuring mission (TRMM) sensor package. *J. Atmos. Oceanic Technol.*, **15**, 809–817.

– –, Y. Hong, W. S. Olson, S. Yang, R. F. Adler, J. McCollum, R. Ferraro, G. Petty, D.-B. Shin, and T. T. Wilheit, 2001: The evolution of the Goddard Profiling Algorithm (GPROF) for rainfall estimation from passive microwave sensors. *J. Appl. Meteor.*, **40**, 1801–1820.

– –, W. S. Olson and L. Giglio, 1996: A simplified scheme for obtaining precipitation and vertical hydrometeor profiles from passive microwave sensors. *IEEE Trans. Geosci. Remote Sens.*, **34**, 1213–1232.

Liebe, H. J., G. A. Hufford and T. Manabe, 1991: A model for the complex permittivity of water at frequencies below 1 THz. *Int. J. Infrared and Millimeter Waves*, **12**, 659–675.

Marshall, J. S. and W. M. Palmer, 1948: The distribution of raindrops with size. *J. Meteor.*, **5**, 165–166.

Marzano, F. S., E. Fionda, P. Ciotti, and A. Martellucci, 2002: Ground-based multifrequency microwave radiometry for rainfall remote sensing. *IEEE Trans. Geosci. Remote Sens.*, **40**, 742–759.

Marzano, F. S., A. Mugnai, G. Panegrossi, N. Pierdicca, E. A. Smith, and J. Turk, 1999: Bayesian estimation of precipitating cloud parameters from combined measurements of spacebrone microwave radiometer and radar. *IEEE Trans. Geosci. Remote Sens.*, **37**, 596–613.

Nzeukou A. and H. Sauvageot, 2002: Distribution of rainfall parameters near the coasts of France and Senegal. *J. Appl. Meteor.*, **41**, 69–82.

Olson, W. S., C. D. Kummerow, G. M. Heymsfield and L. Giglio, 1996: A method for combined passive-active microwave retrievals of cloud and precipitation profiles. *J. Appl. Meteor.*, **35**, 1763–1789.

Olson, W. S., C. D. Kummerow, S. Yang, G. W. Petty, W.-K. Tao, T. L. Bell, S. A. Braun, Y. Wang, S. E. Lang, D. E. Johnson, and J. C. Chiu, 2005: Precipitation and latent heating distributions from satellite passive microwave radiometry. Part I: Improved method and Uncertainties. *J. Appl. Meteor.* (accepted)

Petty, G. W., 1994a: Physical retrievals of over-ocean rain rate from multichannel microwave imagery. Part I: Theoretical characteristics of normalized polarization and scattering indices. *Meteorol. Atmos. Phys.*, **54**, 79–100.

Petty, G. W., 1994b: Physical retrievals of over-ocean rain rate from multichannel microwave imagery. Part II: Algorithm implementation. *Meteorol. Atmos. Phys.*, 54(1-4), 101–121.

Sauvageot, H., 1994: The probability density function of rain rate and the estimation of rainfall by area integrals. . *J. Appl. Meteor.*, **33**, 1255–1262.

Swift, J. L. W., and H. T. Schreuder, 1981: Fitting daily precipitation amounts using the Sb distribution. *Mon. Wea.. Rev.*, **109**, 2535–2540.

Tassa, A., S. Di Michele, F. S. Marzano, A. Mugnai, and J. P. V. P. Baptista, 2003: Cloud-model based Bayesian technique for precipitation profile retrieval from TRMM microwave imager. *Radio Sci.*, **38**, 8074–.

Wilheit, T. T., 1986: Some comments on passive microwave measurement of rain. *Bull. Amer. Meteor. Sci.*, **67**, 1226–1232.

Wilks, D. S., and K. L. Eggleston, 1992: Estimating monthly and seasonal precipitation distributions using the 30- and 90- day outlooks. *J. Climate*, **5**, 252–259.

Table Captions

Table 1. Parameters a and b in the approximation of liquid water extinction coefficient.

Table 2. Coefficients of a_μ, b_μ, and c_μ.

Table 3. Information of designed experiments in sensitivity tests, including the experiment ID, the training dataset, and the specifications of the prior and conditional likelihoods applied to the Bayesian algorithm.

Table 4. Bias, root-mean-squared difference(RMSD), and correlation coefficients (Corr) for each algorithm and each validation dataset. The unit of bias and RMSD is mm/hr.

Tables

Table 1. Parameters a and b in the approximation of liquid water extinction coefficient.

Channel (GHz)	$\kappa_{e,l}$ (m^2/kg)	a	b
10.65	0.0244	0.002956	1.18759
19.35	0.0785	0.01585	1.09403
37.00	0.261	0.06896	1.01876
85.50	0.932	0.2799	0.84693

Table 2. Coefficients of a_μ, b_μ, and c_μ.

Channel (GHz)	a_μ	b_μ	c_μ
10.65	0.75	0.03	0.30
19.35	1.35	0.05	-0.30
37.00	1.55	0.10	-0.50

Table 3. Information of designed experiments in sensitivity tests, including the experiment ID, the training dataset, and the specifications of the prior and conditional likelihoods applied to the Bayesian algorithm.

Experiment ID	$\pi(R)$	Physical model
R0	logN(0,2)	Nonlinear model from (17) – (19)
R1	logN(0,1)	Nonlinear model from (17) – (19)
R2	Uniform [0, 100]	Nonlinear model from (17) – (19)
R3	logN(0,2)	Different parameterizations in (19)
R4	logN(0,2)	Linear model from (13) – (16)

Table 4. Bias, root-mean-squared difference (RMSD), and correlation coefficients (Corr) for each algorithm and each validation dataset. The unit of bias and RMSD is mm/hr.

	Orbit 336			Bauer's cases			April 1998		
	Bias	RMSD	Corr	Bias	RMSD	Corr	Bias	RMSD	Corr
GPROF	-0.22	2.68	0.88	-0.22	1.64	0.76	-0.21	1.18	0.78
Linear model	-0.29	2.71	0.88	0.00	1.58	0.78	-0.08	1.09	0.81
Bayesian-MEAN	0.00	2.89	0.85	0.08	1.84	0.71	0.03	1.26	0.78
Bayesian-MLE	-1.04	3.75	0.85	-0.29	1.80	0.74	-0.01	1.21	0.75

Figure Captions

Fig. 1. Contours of the number of pixels based on TMI data (the first and the third columns). Contours are logarithmically spaced; actual value is 10^x, where x is the contour label. x are plotted for values of [0.5, 1, 2, 3, 4,5].

Fig. 2. Examples of derived posterior rain rate distributions at some given P vectors in experiment R0. The observation vector (P_{10}, P_{19}, P_{37}) is presented by the three numbers in parentheses.

Fig. 3. Histograms of retrievals at different rain rate ranges for R0 experiment. Titles contain information about range of true values RR, sample size, and the estimator. Numbers in parentheses are the mean and standard deviation of the histogram. Percentages are the fractions of retrieved rain rates located in the correct range.

Fig. 4. Same as Fig. 3, but using MLE estimations.

Fig. 5. Retrieval histogram of experiment R1 at rain rate ranges of [2, 4], [15, 30], and [50, 75] mm/hr for MEAN (upper panel) and MLE (bottom panel).

Fig. 6. Joint PDFs of the P vector for experiment R0 (upper panel) and R4 (bottom panel). Contours are plotted for [0.05, 0.5, 1.0, 2.5, 5.0, 7.5, 10].

Fig. 7. Same as Fig. 3, but for experiment R4.

Fig. 8. (a) PR interpolated rain rates with a 15-km resolution for TRMM/TMI orbit 336. Retrieved rain rate (mm/hr) from (b) GPROF, (c) the linear model algorithm, (d) Bayesian-MEAN, and (e) Bayesian-MLE models for TRMM/TMI orbit 336.

Fig. 9. Scatter plot of retrieved rain rate vs. PR rain rate for all algorithms for TMI orbit 336.

Fig. 10. Posterior PDFs of retrieved rain rates at locations A, B, C, and D that are marked in Fig. 8(d).

Fig. 11. 2-D distribution of Heidke skill scores (HSS) for the 12 selected cases from the Bauer et al. (2001). Retrieval algorithms are: (a) GPROF, (b) the linear model, (c) Bayesian-MEAN, and (d) Bayesian-MLE. The value noted in the bottom-right corner of each plot indicates the highest HSS of the algorithm. Contours are plotted with an interval of 0.1.

Fig. 12. Plots of the best algorithm rain rate threshold with respect to the threshold of PR rain rate for the Bauer's cases with (a) GPROF, (b) the linear model, (c) Bayesian-MEAN, and (d) Bayesian-MLE.

Fig. 13. Plots of the maximum Heidke skill score vs. the PR rain rate threshold in the range of [0, 10] mm/hr for Bauer's cases.

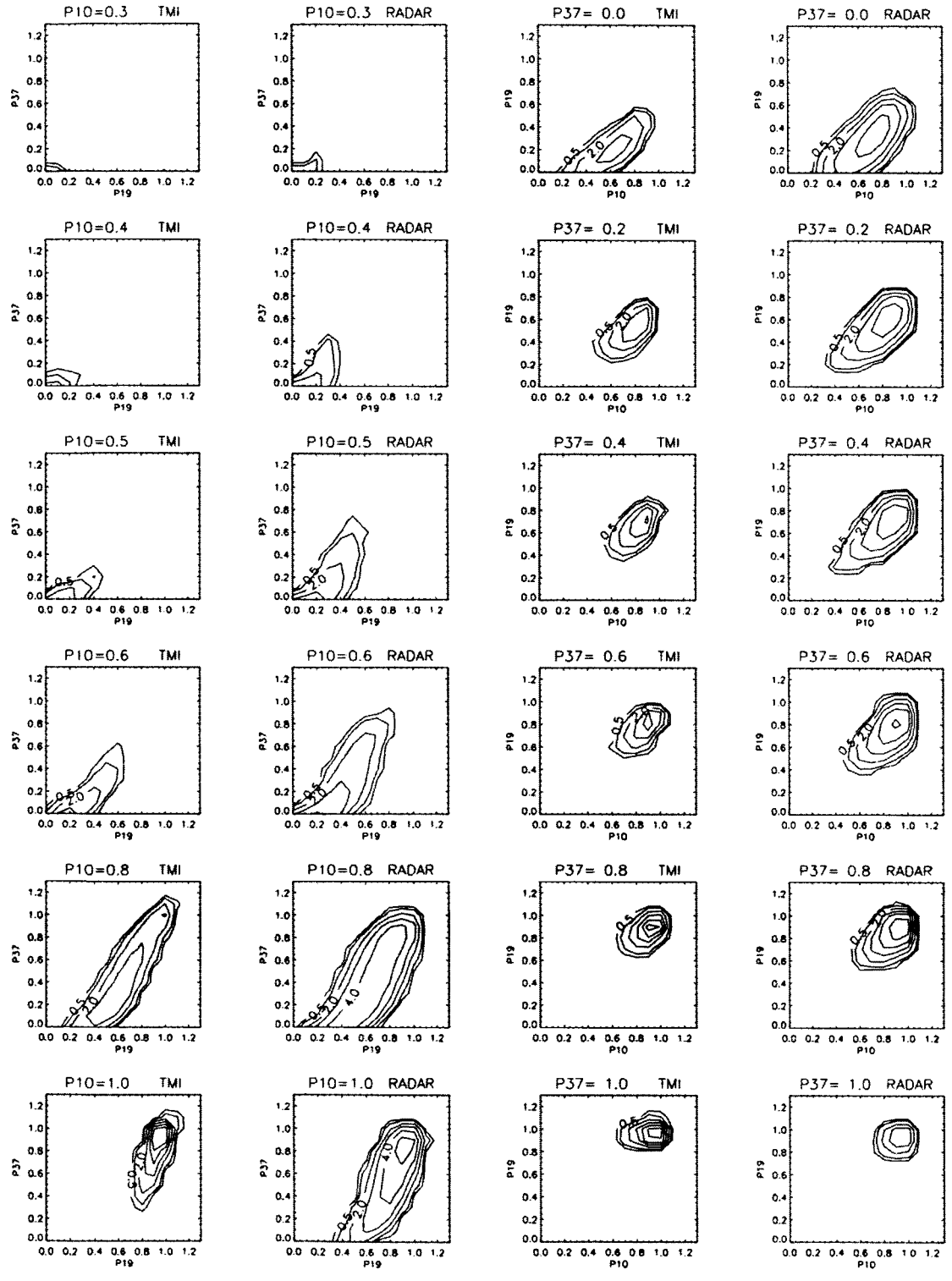

Fig. 1. Contours of the number of pixels based on TMI data (the first and the third columns). Contours are logarithmically spaced; actual value is 10^x, where x is the contour label. x are plotted for values of [0.5, 1, 2, 3, 4,5].

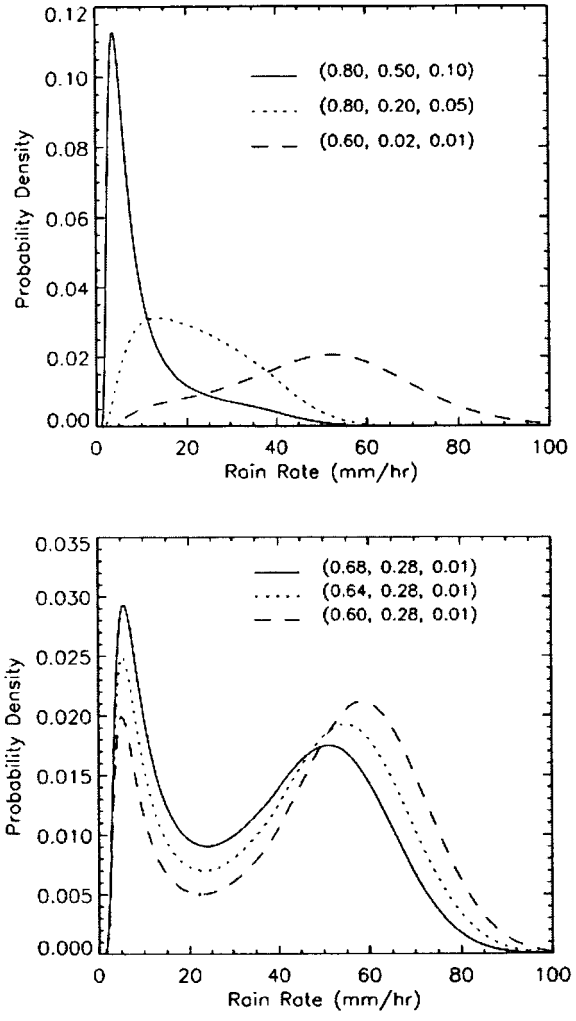

Fig. 2. Examples of derived posterior rain rate distributions at some given P vectors in experiment R0. The observation vector (P_{10}, P_{19}, P_{37}) is presented by the three numbers in parentheses.

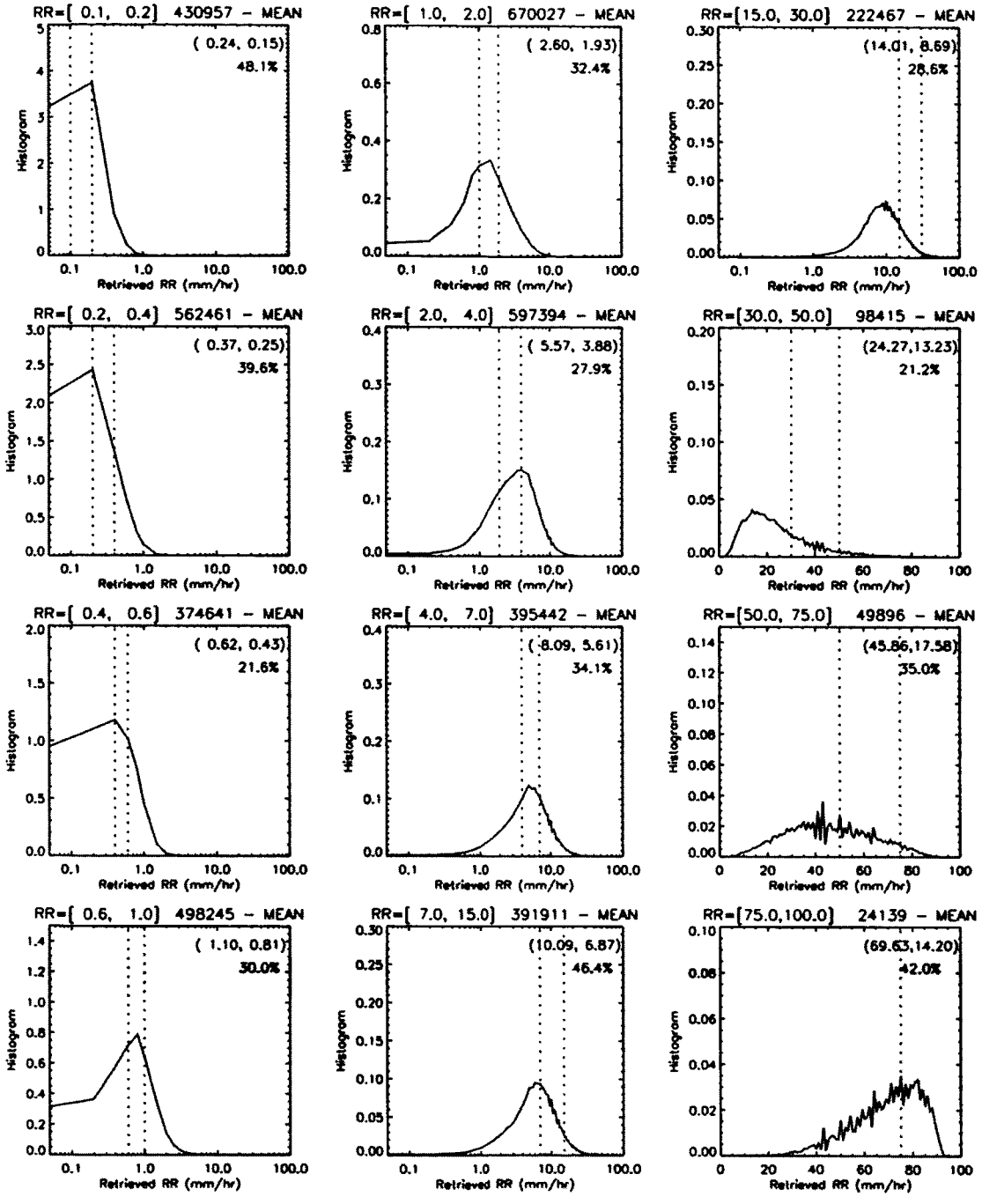

Fig. 3. Histograms of retrievals at different rain rate ranges for R0 experiment. Titles contain information about range of true values RR, sample size, and the estimator. Numbers in parentheses are the mean and standard deviation of the histogram. Percentages are the fractions of retrieved rain rates located in the correct range.

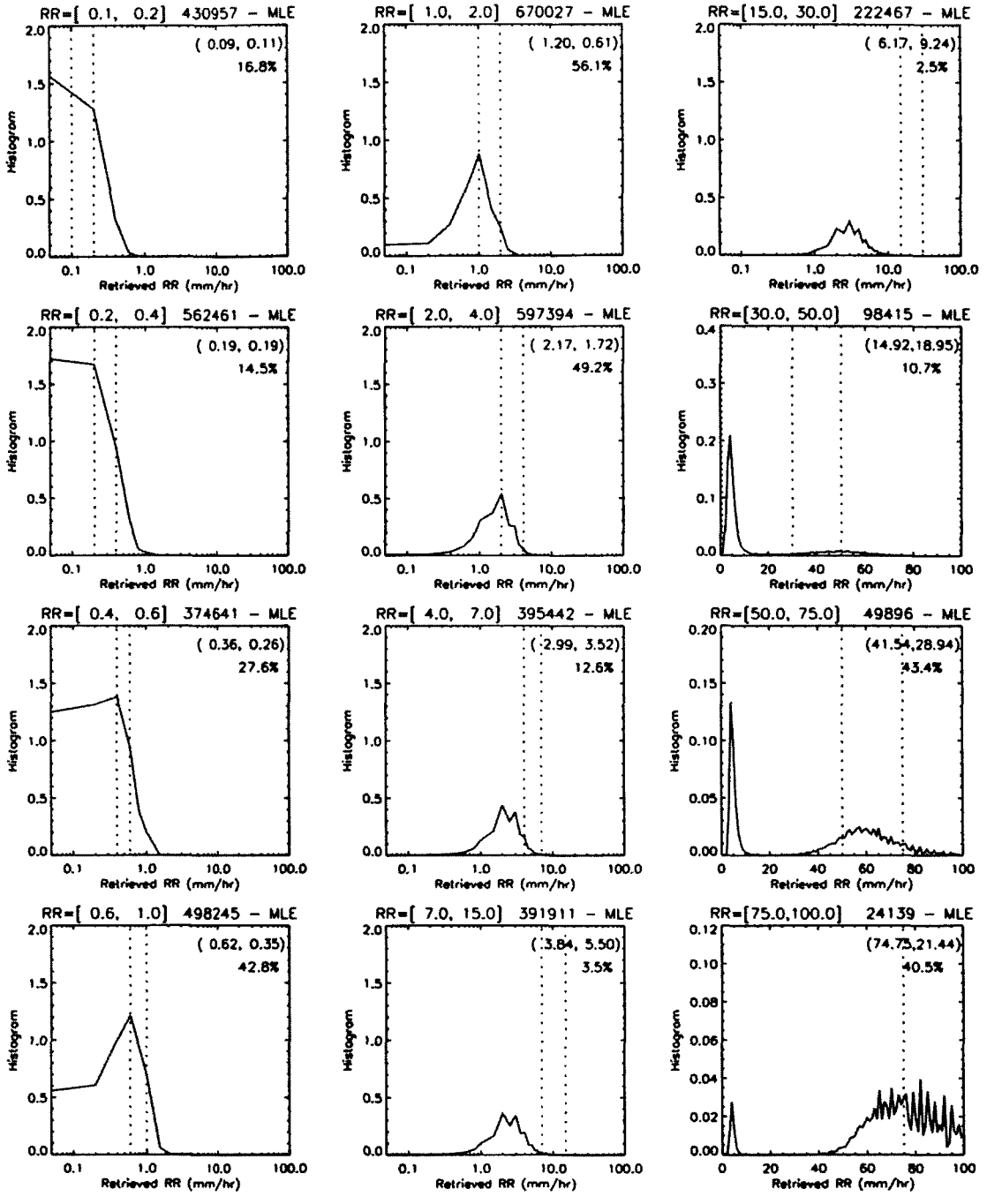

Fig. 4. Same as Fig. 3, but using MLE estimations.

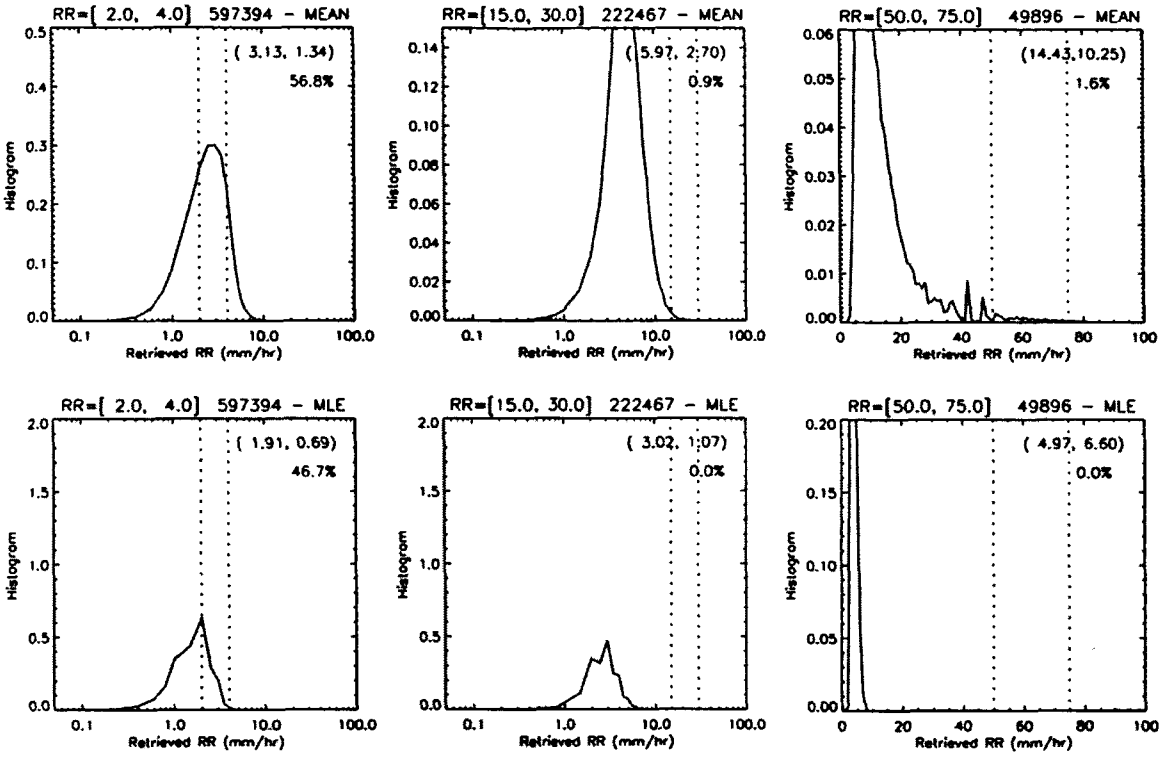

Fig. 5. Retrieval histogram of experiment R1 at rain rate ranges of [2, 4], [15, 30], and [50, 75] mm/hr for MEAN (upper panel) and MLE (bottom panel).

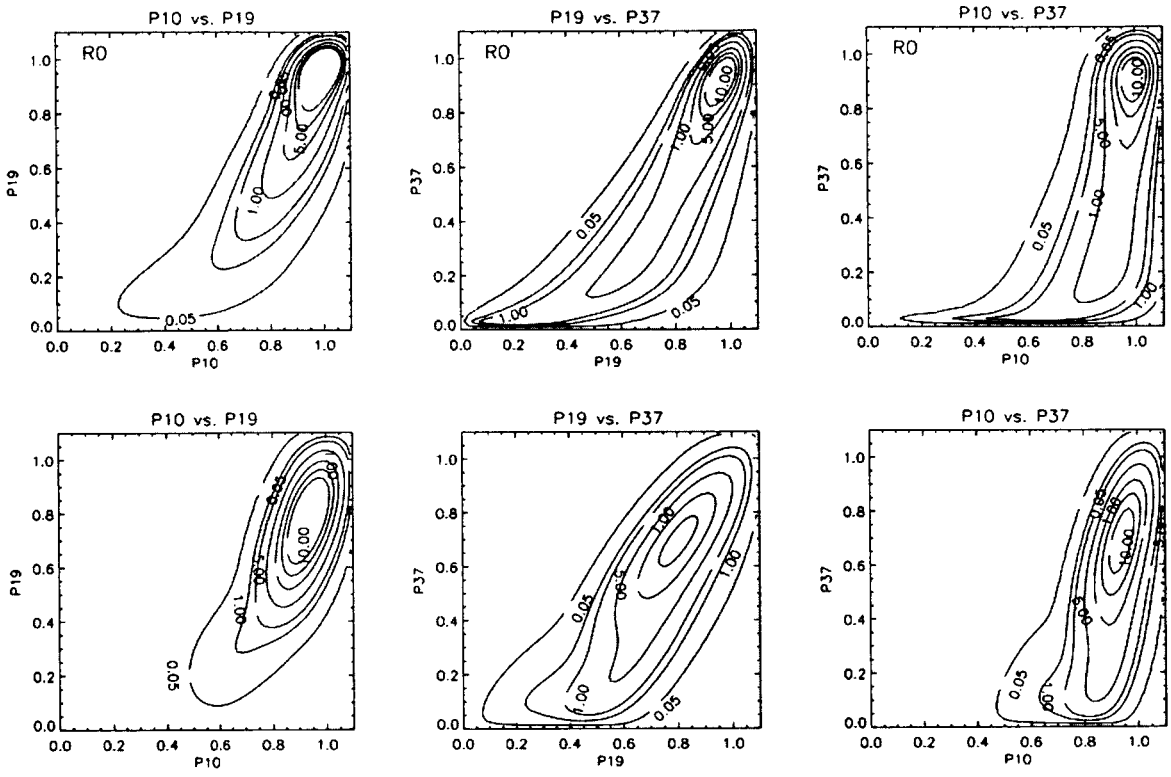

Fig. 6. Joint PDFs of the *P* vector for experiment R0 (upper panel) and R4 (bottom panel). Contours are plotted for [0.05, 0.5, 1.0, 2.5, 5.0, 7.5, 10].

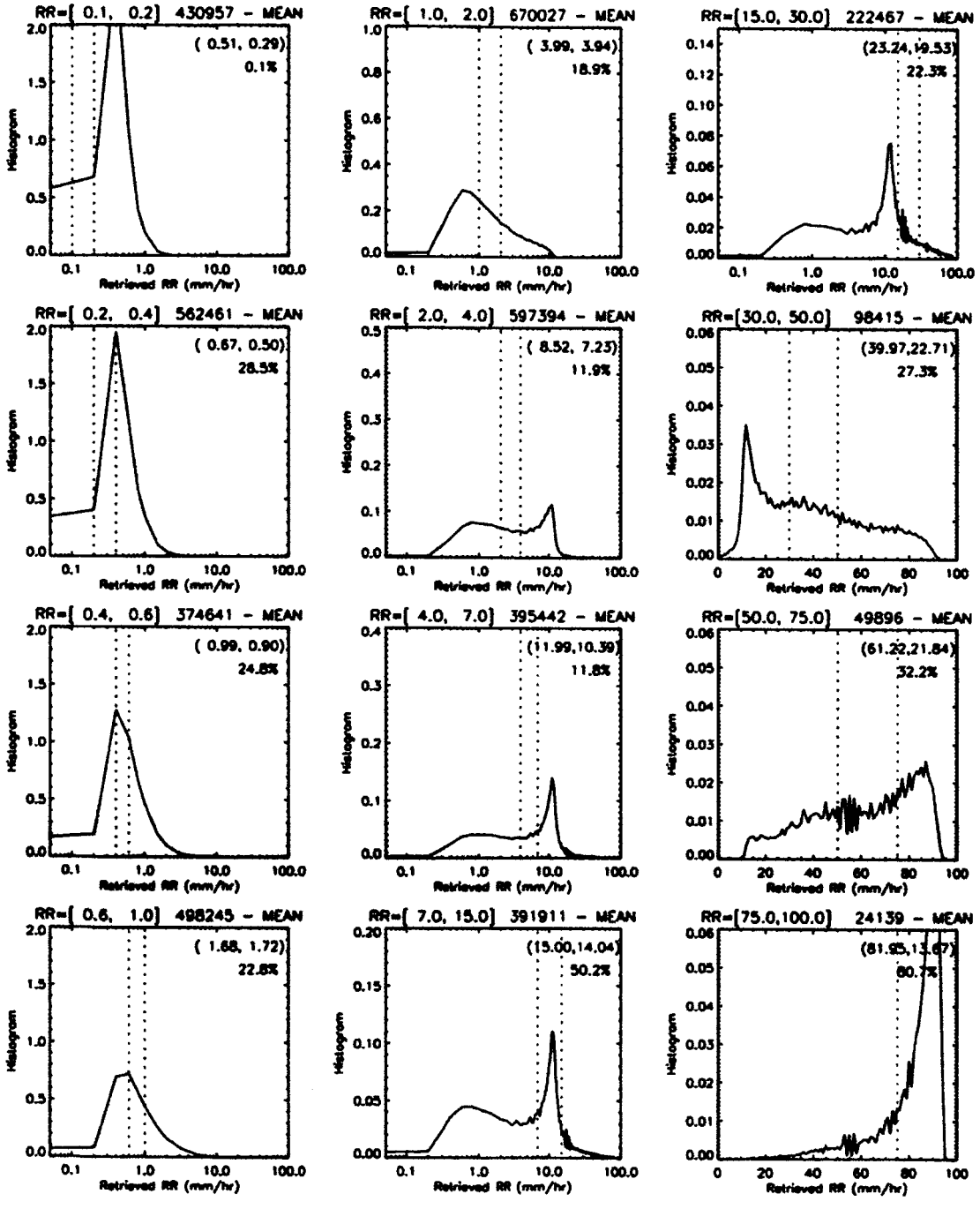

Fig. 7. Same as Fig. 3, but for experiment R4.

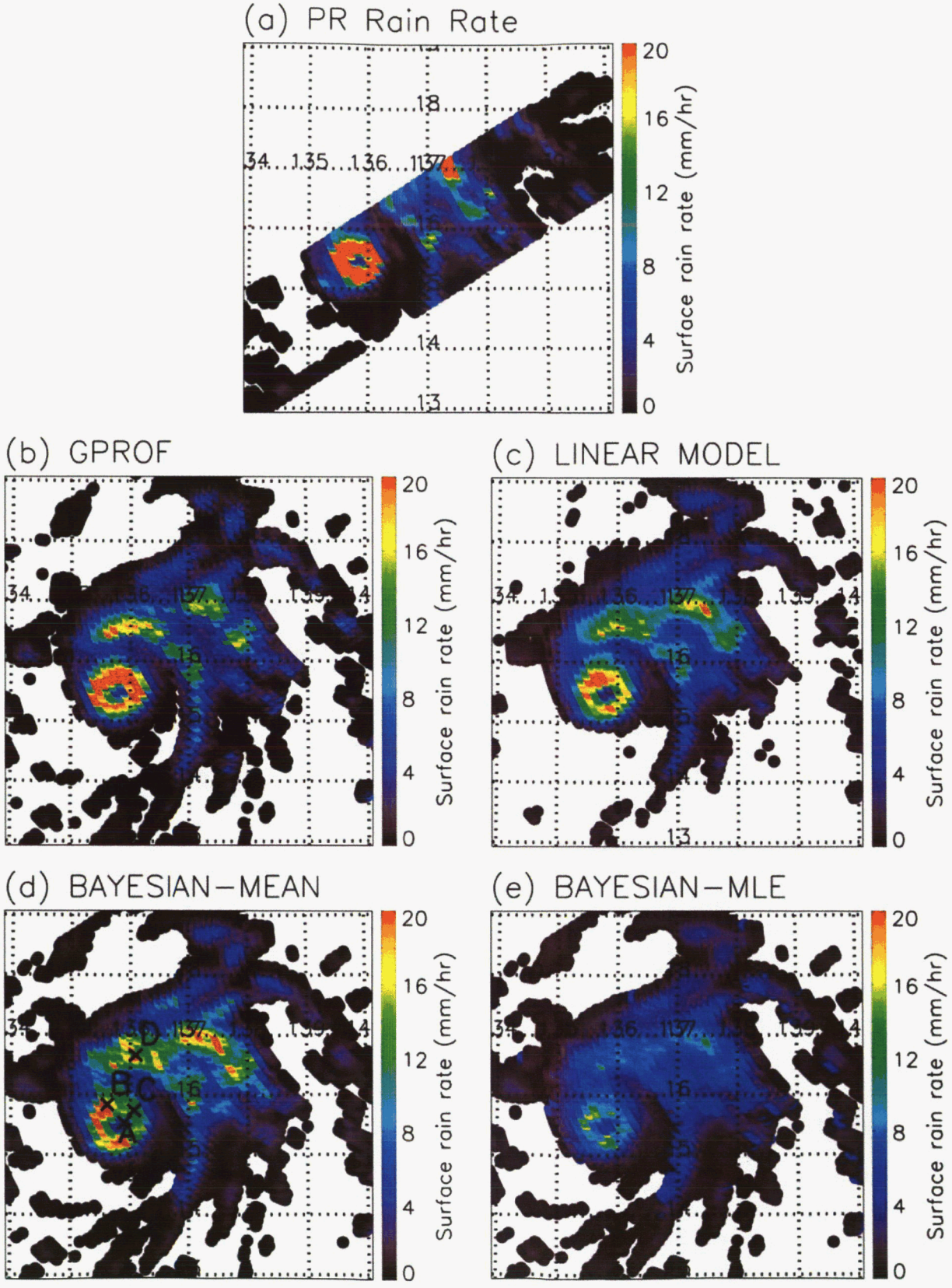
(a) PR Rain Rate
(b) GPROF
(c) LINEAR MODEL
(d) BAYESIAN−MEAN
(e) BAYESIAN−MLE
Surface rain rate (mm/hr)
20
16
12
8
4
0
A
B
C
D

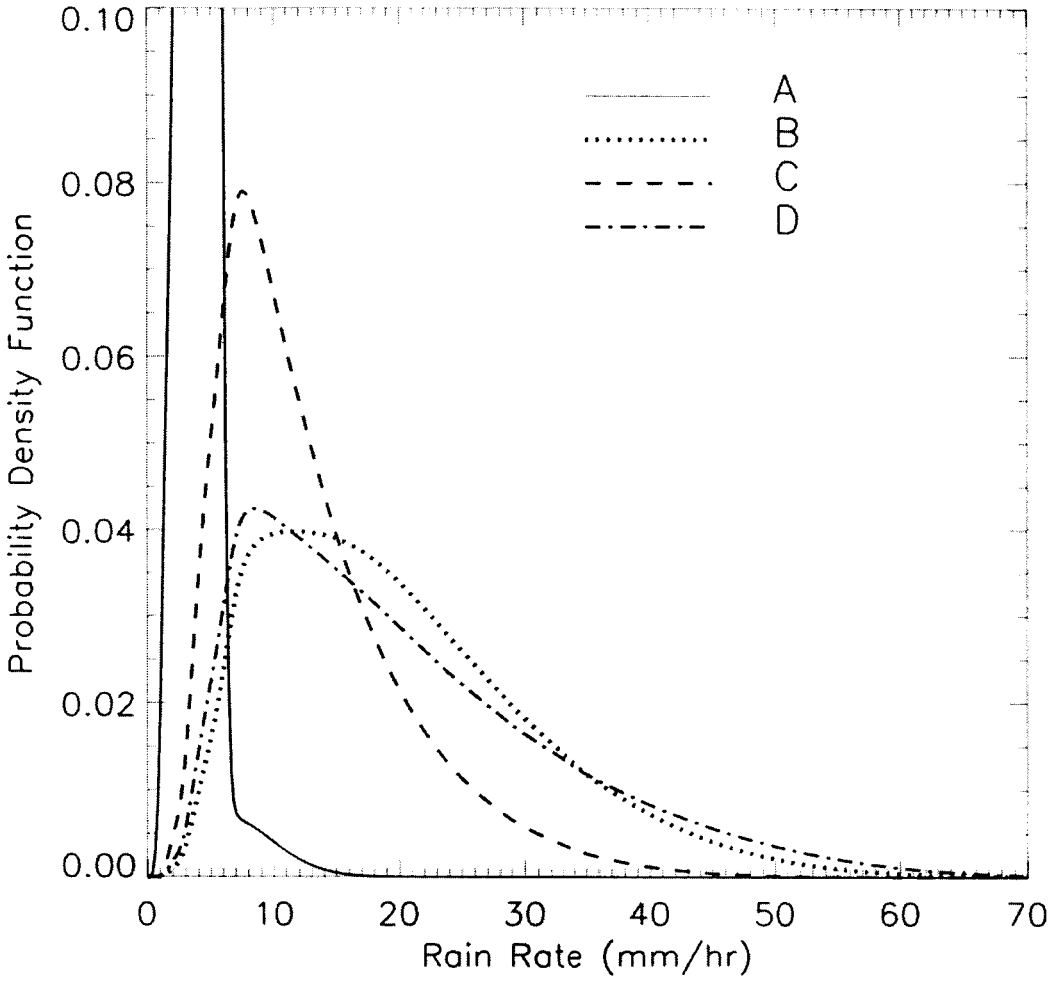

Fig. 10. Posterior PDFs of retrieved rain rates at locations A, B, C, and D that are marked in Fig. 8(d).

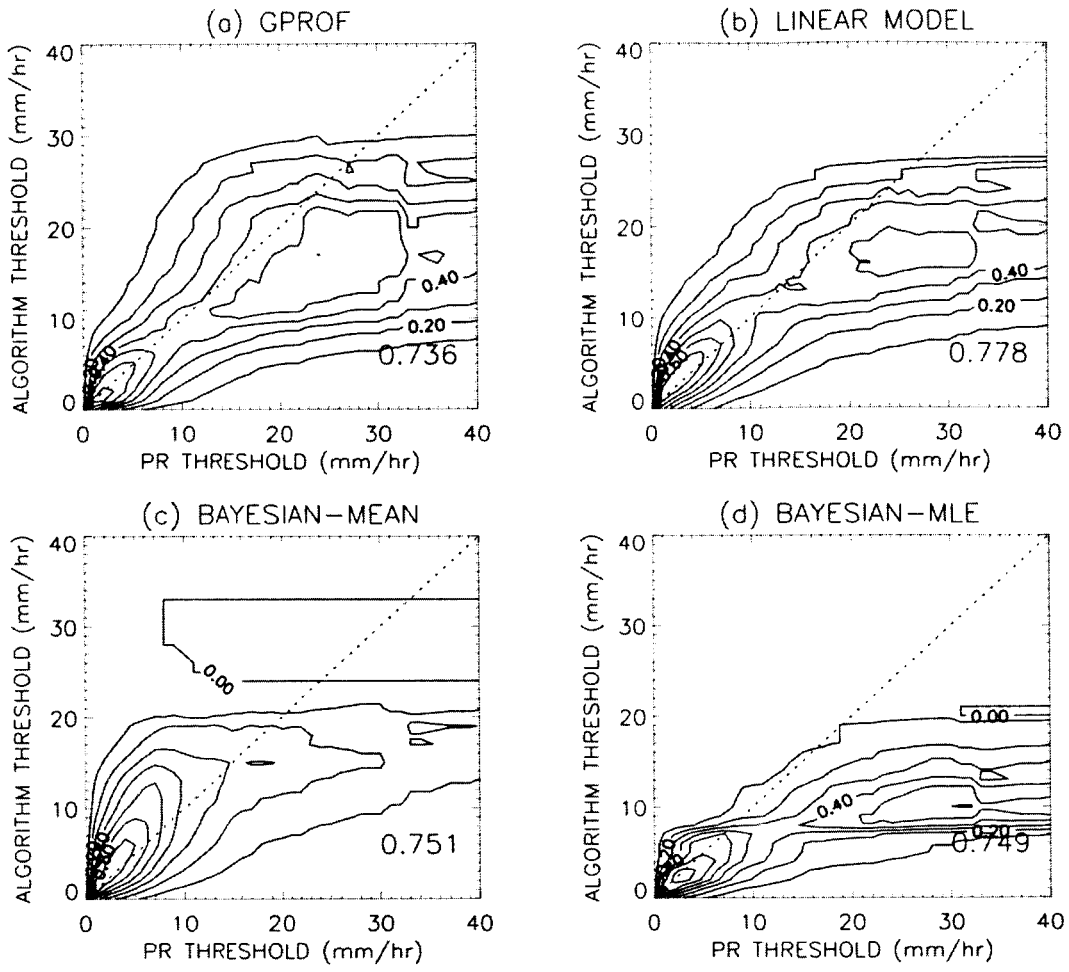

Fig. 11. 2-D distribution of Heidke skill scores (HSS) for the 12 selected cases from the Bauer et al. (2001). Retrieval algorithms are: (a) GPROF, (b) the linear model, (c) Bayesian-MEAN, and (d) Bayesian-MLE. The value noted in the bottom-right corner of each plot indicates the highest HSS of the algorithm. Contours are plotted with an interval of 0.1.

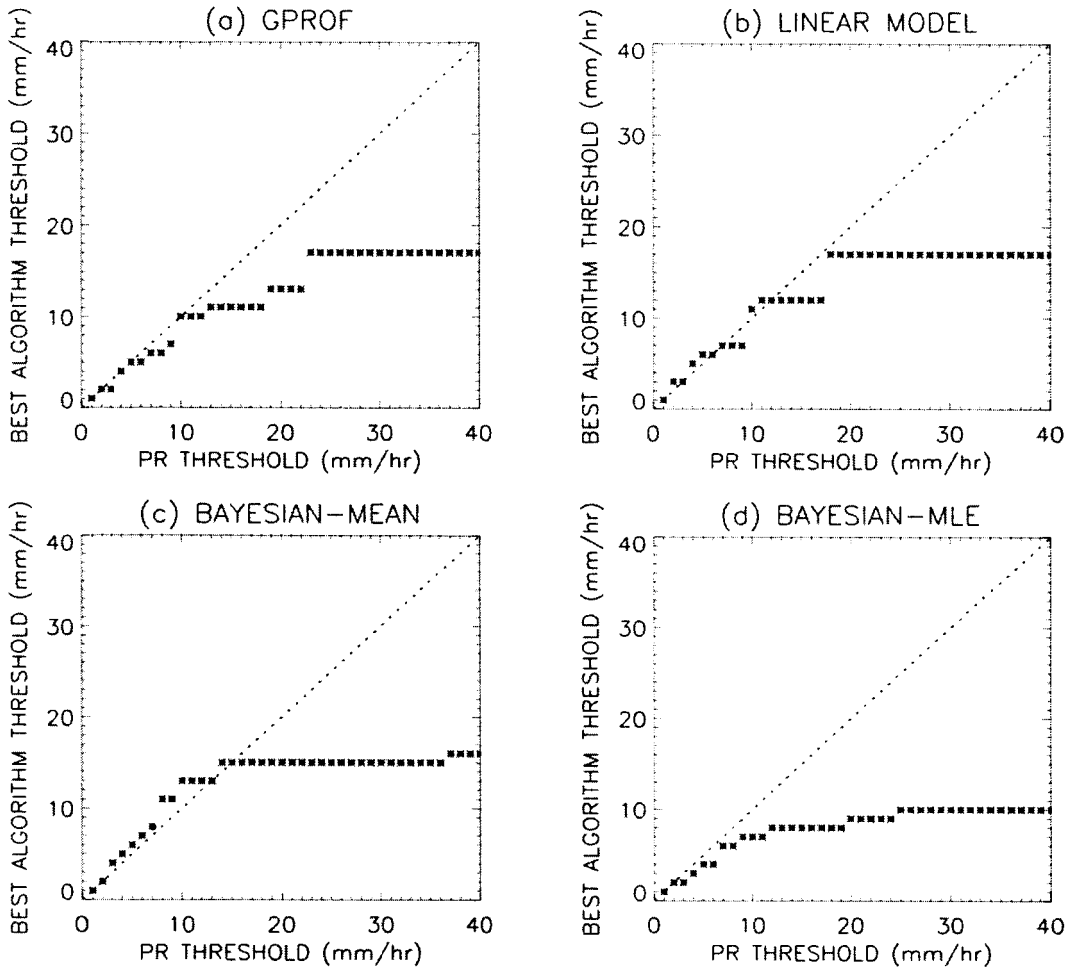

Fig. 12. Plots of the best algorithm rain rate threshold with respect to the threshold of PR rain rate for the Bauer's cases with (a) GPROF, (b) the linear model, (c) Bayesian-MEAN, and (d) Bayesian-MLE.

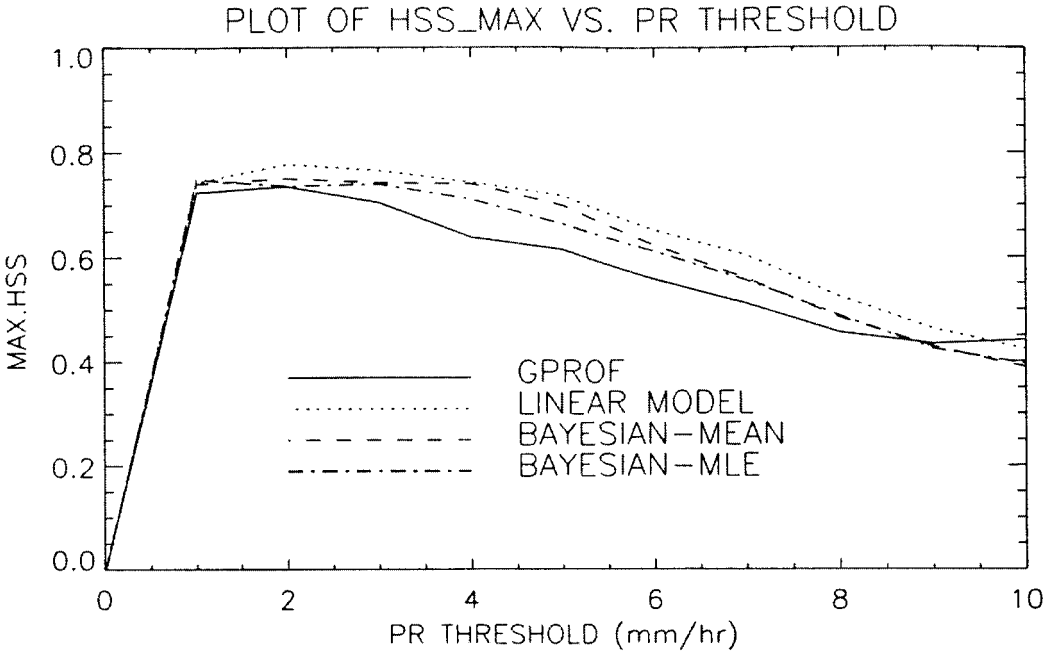

Fig. 13. Plots of the maximum Heidke skill score vs. the PR rain rate threshold in the range of [0, 10] mm/hr for Bauer's cases.

Fig. 8. (a) PR interpolated rain rates with a 15-km resolution for TRMM/TMI orbit 336. Retrieved rain rate (mm/hr) from (b) GPROF, (c) the linear model algorithm, (d) Bayesian-MEAN, and (e) Bayesian-MLE models for TRMM/TMI orbit 336.

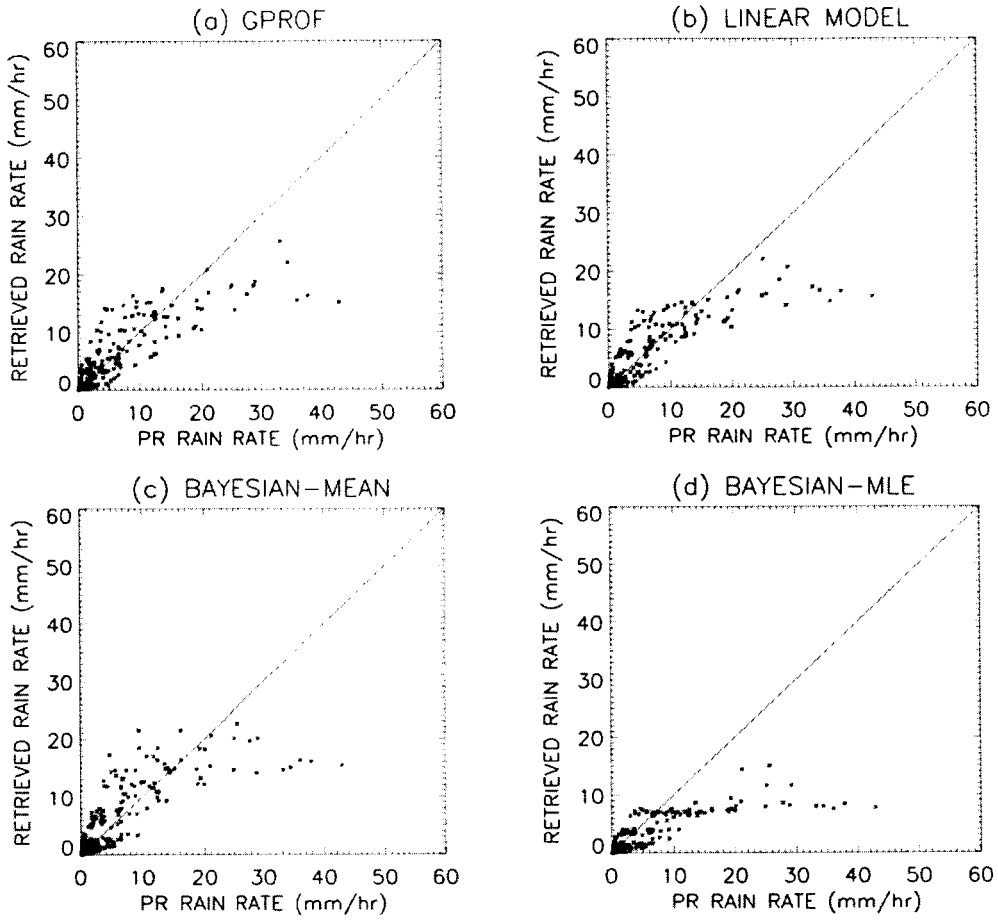

Fig. 9. Scatter plot of retrieved rain rate vs. PR rain rate for all algorithms for TMI orbit 336.

"Bayesian Retrieval of Complete Posterior PDFs of Oceanic Rain Rate From Microwave Observations"

J. Christine Chiu (JCET) and Grant W. Petty (Univ. of ~~Washington~~ Wisconsin)

accepted by J. Applied Meteorology

Popular Summary

Precipitation is an essential element in the quantitative understanding of the global hydrological cycle. Global surface rainfall is now widely estimated from satellite passive microwave observations. Inference of surface rainfall from microwave radiation would be less troublesome if the relationship between these two variables were unique and reasonably linear. Unfortunately, not only is the relationship non-monotonic owing to the competing effects of scattering and emission, but a variety of microphysical and environmental factors introduces significant variability into the relationship.

Bayes' theorem offers a rigorous and completely general theoretical framework for retrieving atmospheric variables from remote sensing measurements. We have fully exploited this theorem, and introduced a new Bayesian algorithm for retrieving surface rain rate from Tropical Rainfall Measurements Mission (TRMM) Microwave Imager over the ocean. While other rain rate algorithms have been published that are based at least partly on Bayesian reasoning, this is believed to be the first self-contained algorithm that yields not just a single "best" estimate of rain rate, but rather a continuous posterior probability distribution of rain rate at any location.

We used synthetic datasets to clarify the theoretical advantage of the Bayesian algorithm, as well as to demonstrate its retrieval ability when imperfect information was applied to the algorithm, which is often the case in reality. We have found that even when perfect knowledge is used, biased retrievals may occur at high rain rates. This bias is not the result of a defect of the Bayesian formalism but rather represents the expected outcome when the physical constraint imposed by the radiometric observations is weak, due to saturation effects.

For real-world applications, we validated rain rate retrievals against estimates from the TRMM Precipitation Radar. The performance of our Bayesian algorithm is found to be comparable to that of other benchmark algorithms, while having the additional advantage of providing a complete continuous posterior probability distribution of surface rain rate.